Article

Neuron

Vascular Compartmentalization of Functional Hyperemia from the Synapse to the Pia

Highlights

- Odor triggers rapid Ca^{2+} elevations in OPC process that are input specific
- All pericyte subtypes and SMCs respond to downstream synaptic activation
- Synchronous mural cell activation is associated with heterogeneous local hemodynamics
- The arteriole and first-order capillary dilate first and form the primary functional unit

Authors

Ravi L. Rungta,
Emmanuelle Chaigneau,
Bruno-Félix Osmanski, Serge Charpak

Correspondence

ravi.rungta@parisdescartes.fr (R.L.R.),
serge.charpak@parisdescartes.fr (S.C.)

In Brief

Rungta et al. perform *in vivo* two-photon calcium imaging of neuron, oligodendrocyte precursor cell, pericyte, and smooth muscle cell responses to olfactory sensory stimulation in combination with vessel diameter and red blood cell velocity measurements along the entire vascular arbor.

Rungta et al., 2018, Neuron *99*, 362–375
July 25, 2018
https://doi.org/10.1016/j.neuron.2018.06.012

CellPress

CellPress

Neuron
Article

Vascular Compartmentalization of Functional Hyperemia from the Synapse to the Pia

Ravi L. Rungta,[1,*] Emmanuelle Chaigneau,[1] Bruno-Félix Osmanski,[1] and Serge Charpak[1,2,*]
[1]INSERM U1128, Laboratory of Neurophysiology and New Microscopy, Université Paris Descartes, Paris 75006, France
[2]Lead Contact
*Correspondence: ravi.rungta@parisdescartes.fr (R.L.R.), serge.charpak@parisdescartes.fr (S.C.)
https://doi.org/10.1016/j.neuron.2018.06.012

SUMMARY

Functional hyperemia, a regional increase of blood flow triggered by local neural activation, is used to map brain activity in health and disease. However, the spatial-temporal dynamics of functional hyperemia remain unclear. Two-photon imaging of the entire vascular arbor in NG2-creERT2;GCaMP6f mice shows that local synaptic activation, measured via oligodendrocyte precursor cell (OPC) Ca^{2+} signaling, generates a synchronous Ca^{2+} drop in pericytes and smooth muscle cells (SMCs) enwrapping all upstream vessels feeding the activated synapses. Surprisingly, the onset timing, direction, and amplitude of vessel diameter and blood velocity changes vary dramatically from juxta-synaptic capillaries back to the pial arteriole. These results establish a precise spatial-temporal sequence of vascular changes triggered by neural activity and essential for the interpretation of blood-flow-based imaging techniques such as BOLD-fMRI.

INTRODUCTION

Human brain mapping largely uses changes in blood flow to map evoked and resting brain activation (Iadecola, 2017; Raichle and Mintun, 2006). However, similar to the propagation of vasomotor responses along peripheral vessels (Emerson and Segal, 2000; Krogh et al., 1922; Segal and Duling, 1986; Welsh et al., 2018), in the brain, synaptic activation triggers a local signal that propagates backward along the vascular tree, resulting in dilation of upstream arterioles (Chen et al., 2014; Iadecola et al., 1997; Longden et al., 2017). Importantly, these upstream arterioles irrigate a volume larger than that of the activated synapses, decreasing the selectivity of vascular responses (O'Herron et al., 2016). In addition to arterioles, large capillaries enwrapped by pericytes, which were initially shown to dilate *in vitro* (Peppiatt et al., 2006), also dilate *in vivo* following synaptic activation (Biesecker et al., 2016; Mishra et al., 2016; Hall et al., 2014; Kisler et al., 2017; Kornfield and Newman, 2014). However, the types of pericytes that respond to synaptic activation with respect to their location on the vascular tree, as well as the site and timing of dilation initiation, are highly controversial (Attwell et al., 2016; Fernández-Klett et al., 2010; Grant et al., 2017; Hall et al., 2014; Hill et al., 2015; Kisler et al., 2017; Mishra et al., 2016; Tian et al., 2010; Wei et al., 2016). A key problem is that these studies have generally assumed that the vascular compartment that regulates blood flow is controlled by the local activation of neurons but have failed to locate the precise site of neuronal activation in their *in vivo* preparations. Furthermore, dilation is thought to be an indication of the timing of local neuronal activation, yet the time of signaling to the vasculature (pericyte or smooth muscle cell [SMC] activation) has not been measured. We hypothesize that the hemodynamics underlying functional hyperemia are complex, and their analysis requires precise measurements of vessel diameter and blood velocity in all the vascular compartments upstream of the capillaries adjacent to activated synapses. Here, by exploiting the unique neural-vascular anatomy of the olfactory bulb (Shepherd, 2003; Tiret et al., 2009) in chronic NG2-creERT2;GCaMP6f mice and back tracing from the few capillaries irrigating activated synapses within a single glomerulus to the pial arteriole feeding them, we precisely measure the timing of neuronal, pericyte, and smooth muscle cell activation as well as the timing of the resulting vessel diameter and blood velocity changes in different vascular compartments.

RESULTS

Synaptic Activity Triggers Odor-Specific OPC Process Ca^{2+} Elevations *In Vivo*

Odors selectively activate olfactory sensory neurons (OSNs) whose terminals converge in individual glomeruli that, when activated, trigger blood flow and velocity increases in local capillaries (Chaigneau et al., 2007; Lecoq et al., 2009). Imaging was performed in NG2creERT2;GCaMP6f mice in which oligodendrocyte precursor cells (OPCs), in addition to pericytes and SMCs, express GCaMP6f (Huang et al., 2014; Rungta et al., 2017). Because OPCs have been shown to respond to neuronal activity via various mechanisms (Bergles et al., 2000; Jabs et al., 2005; Lin and Bergles, 2004; Maldonado and Angulo, 2015; Stevens et al., 2002), we tested whether glomerular OPCs responded to odor and could potentially be used as markers of synaptic activation. Non-mural cells expressing GCaMP6f were detected in the glomerular layer, and their identity as OPCs

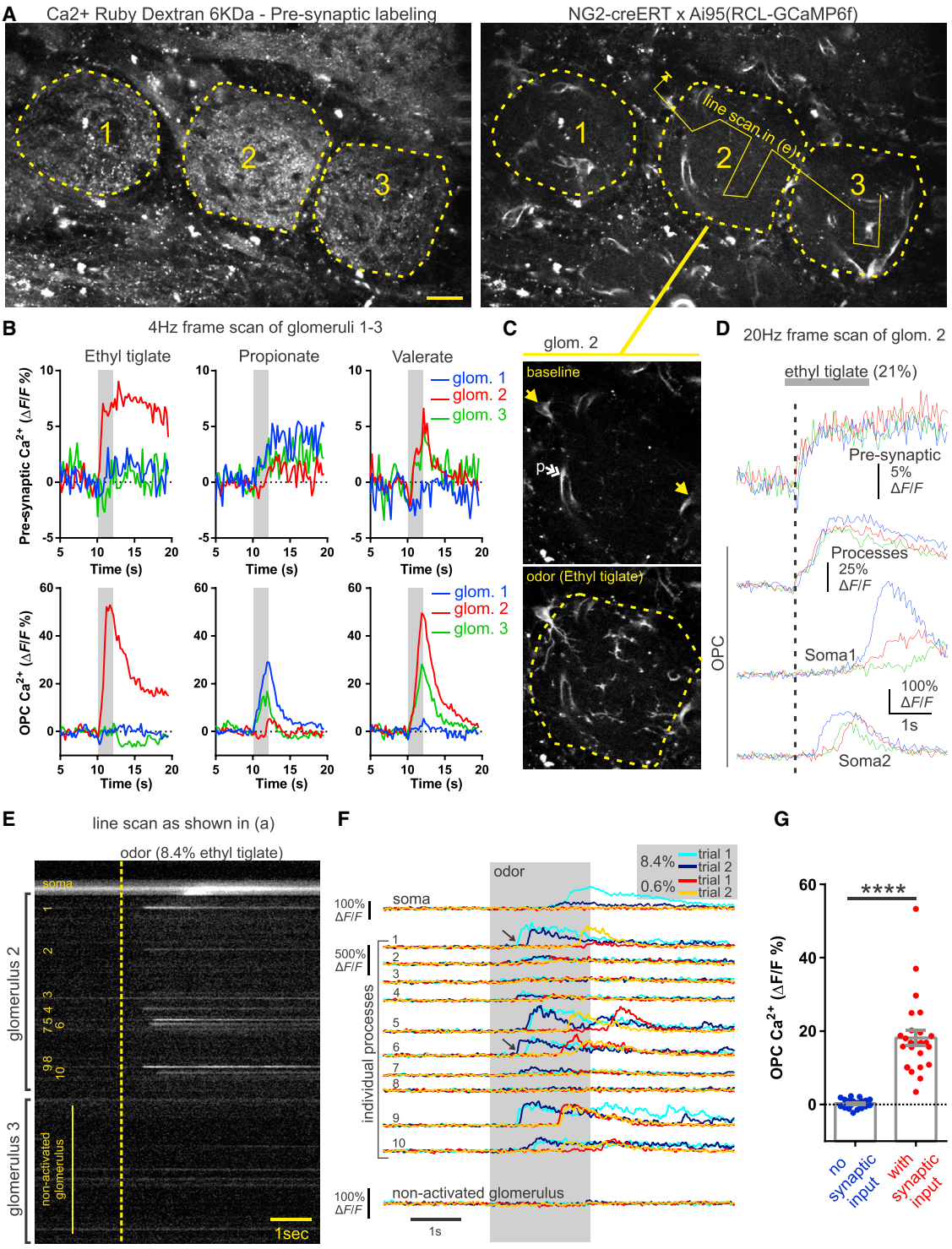

Figure 1. OPC Process Ca^{2+} Elevations Are Rapid and Reliable Markers of Glomerular Synaptic Activation

(A) Image of three glomeruli with OSN terminals loaded with Ca^{2+} Ruby Dextran-6KDa (left) and OPCs and pericytes expressing GCaMP6f under control of the NG2 promoter (right). Dashed lines outline individual glomeruli (1–3), and the solid line arrow indicates path of broken line scan in (E) and (F). Scale bar, 25 μm.

(B) Pre-synaptic OSN terminal (top) and OPC process (bottom) responses in glomeruli 1–3 (imaged simultaneously as shown in A) show matching odor selectivity of pre-synaptic and OPC process Ca^{2+} signals within individual glomeruli.

(C) Image of glomerulus #2 shows GCaMP6f signal at baseline (top) and following inhalation of ethyl tiglate (bottom). Single yellow arrows indicate location of periglomerular OPC somata, and the double white arrow indicates pericytes processes (p).

(legend continued on next page)

was confirmed, as immunostaining showed that these cells were positive for the OPC markers Olig2 and PDGFαR (Figure S1), with processes extending into the neuropil of one or more glomeruli (Figure S1C). To test the glomerular specificity of OPC responses, we simultaneously monitored Ca^{2+} signaling in OSN terminals labeled with Ca^{2+} Ruby nano (red) and in GCaMP6f-expressing OPCs (Figure 1A). In glomeruli in which odor triggered a Ca^{2+} elevation in pre-synaptic terminals, Ca^{2+} also increased in OPC processes (Figures 1B and 1G; Video S1), whereas in glomeruli with no detectable presynaptic Ca^{2+} elevation, the OPC-GCaMP6f signal did not increase (Figures 1B and 1G; Video S1). The onsets of OSN terminal and OPC processes Ca^{2+} elevations were rapid and indistinguishable with the temporal resolution of our movie acquisitions (50–150 ms/frame), whereas when signals were observed in the peri-glomerular OPC somata, they were delayed by several hundred milliseconds (Figures 1C and 1D; mean delay between processes and soma, 699 ± 91 ms, $p < 0.0001$, n = 23, 7 mice). Performing line scans across different OPC processes of the same glomerulus, we observed that the kinetics and amplitude of the Ca^{2+} signals differed between adjacent OPC processes. Additionally, for a given process, the response onset varied from trial to trial and occurred more rapidly at higher odor concentration, which also increased the likelihood of observing somata responses (Figures 1E and 1F). Figure S2 shows that in some processes (e.g., region of interest [ROI] 1), the OPC response was biphasic with an initial elevation that reliably followed the OSN terminal Ca^{2+} signal and a second signal whose onset was variable, whereas in other processes (ROIs 2–4), the fast response was barely detectable and the secondary response very variable. Note that although OSN terminal activation must occur before the OPC activation, we were unable to distinguish these two Ca^{2+} signal onsets, even with line scans acquired at >500 Hz (Figure S2C; mean delay ± SEM, −39 ms ± 64 ms, $p > 0.05$, n = mean responses from 4 mice [112 trials]).

Finally, we tested whether these OPC signals depended on glutamate release by OSN terminals by injecting a cocktail of glutamate receptor antagonists via a glass micro pipette targeted into responsive glomeruli of acutely prepared mice (see STAR Methods) (Figure 2A). Blockade of AMPA, NMDA, and groups 1 and 2 mGluR receptors reversibly blocked the odor-evoked OPC Ca^{2+} signal, whereas injection of control solution had no effect (Figures 2B and 2C). Together, these results demonstrate that OPC process Ca^{2+} elevations can be used as a spatial and temporal marker of glomerular activation. As Ca Ruby labeling was variable between mice, this allowed us to simultaneously monitor glomerular activation and mural cell Ca^{2+} dynamics without the need to label OSN terminals.

Synaptic Activation Triggers Decreased Microdomain Ca^{2+} Signaling and Delayed Ca^{2+} Drops in Thin-Strand Pericytes

Next, we investigated the Ca^{2+} signaling dynamics in capillary pericytes. In the glomerular layer, juxta-synaptic capillaries were located 5–8 branches downstream of parenchymal arterioles, contacted by thin-strand pericytes, and had a mean luminal diameter of 3.7 ± 0.2 μm (n = 14 capillaries, 12 mice). Imaging of these GCaMP6f thin-strand pericytes revealed frequent spontaneous Ca^{2+} elevations within their processes. These spontaneous Ca^{2+} transients were highly localized and largely independent even in sub-regions of the same process separated by few microns (Figures 3A–3C; Video S2). Upstream capillaries closer to the parenchymal arteriole were larger and enwrapped by pericytes, which similarly displayed spontaneous Ca^{2+} transients within microdomains of processes (Figure S3; Video S3). Note that in the current study, we named arterioles all vessels surrounded by a continuous layer of SMCs. All pericyte subtypes responded to odor. In glomeruli in which the onset of synaptic activation was recorded (as a Ca^{2+} elevation in either OSN terminals or OPC processes), we regularly observed a decrease in the frequency of the thin-strand pericyte spontaneous Ca^{2+} transients (3D–3G and 4A; baseline, 0.28 ± 0.02 Hz versus odor, 0.14 ± 0.01 Hz, $p < 0.0001$, n = 12 glomerulus pericytes from 10 mice). This decrease in transient frequency was associated with a slight but significant decrease in the amplitude and duration of the transients measured during the 5 s period following the odor stimulation onset (Figures 3H and 3I; mean amplitude, 90.6% ± 6.2% versus 80.4% ± 6.0% $\Delta F/F$, $p < 0.05$; mean duration, 762 ± 45 versus 600 ± 22 ms, $p < 0.01$, n = 12 glomerulus pericytes from 10 mice). In addition, this decrease in Ca^{2+} transients resulted in an overall decrease in the pericyte Ca^{2+} concentration, which could be evidently detected in the averages from multiple trials (Figures 3F and 4B; Figure S4). Analysis of baseline fluorescence between well-separated Ca^{2+} transients indicated that in addition to an effect on transient frequency, odor also decreased the resting pericyte Ca^{2+} concentration (−7.1% ± 1.4% $\Delta F/F$, $p < 0.001$, n = 12 glomerular pericytes from 10 mice [5–20 trials/pericyte]). Note that the Ca^{2+} drop was not due to changes in cell volume as illustrated in control experiments exciting GcAMP6f at a wavelength where the Ca^{2+} sensitivity was lost (Figure S4). Comparing the average response from all mice showed that the onset of the Ca^{2+} drop did not precede the increase in red blood cell (RBC) velocity (Figure 4A),

(D) Acquisition at higher temporal resolution shows that the onset of the OPC process Ca^{2+} signal occurs rapidly in response to OSN activation; the signal represents the average response within the entire glomerulus, outlined by the dashed line in (C). Bottom two traces show that odor also triggers Ca^{2+} increases in the periglomerular OPC somas that are delayed by several hundred milliseconds.

(E) Line scan acquisition, as drawn in (A) through glomeruli 2 and 3, shows that ethyl tiglate triggers variable Ca^{2+} increases in individual OPC processes and somata from glomerulus 2. Dashed yellow line indicates onset of 2 s odor delivery.

(F) Analysis reveals that responses of individual OPC processes vary from trial to trial (see black arrows) for a given odor stimulation intensity and that the onset and amplitude of the GCaMP6f signals in different processes show variability and are more delayed at lower concentration. The soma signal is dependent on the stimulation intensity.

(G) Summarized data show matching selectivity of pre-synaptic Ca^{2+} and OPC Ca^{2+} in 14 glomeruli from 8 mice. Data represent mean ± SEM.

See Figures S1 and S2 and Video S1.

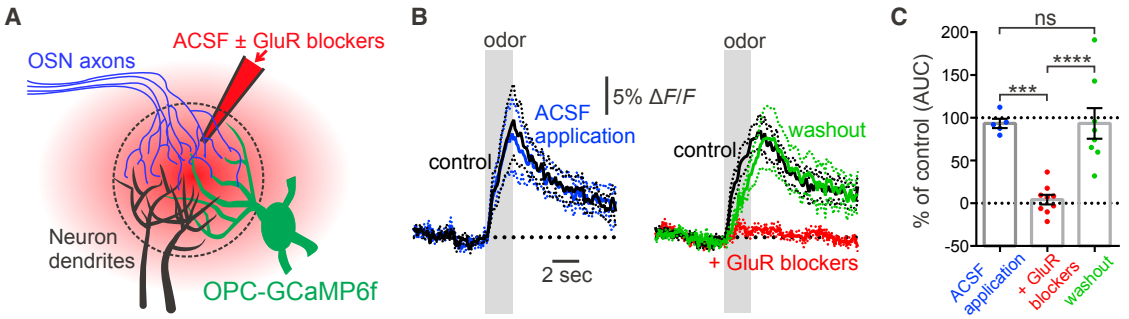

Figure 2. OPC Process Ca^{2+} Elevations Require Glutamate Release

(A) Schematic: control ACSF or ACSF containing GluR blockers (D-APV, 500 μM; NBQX, 300 μM; MPEP, 250 μM; CPCCOEt, 500 μM; LY341495, 100 μM) was locally injected in a glomerulus of acutely prepared mice in combination with Texas red to visualize successful injection of solution.

(B and C) Summarized data showing that injection of ACSF had no effect on the OPC Ca^{2+} signal (B, left), whereas injection of GluR blockers reversibly inhibited the OPC Ca^{2+} elevation (B, right). (B) Time course: gray bars indicate time of odor application. Left: n = 5 glomeruli from 3 mice; right, n = 9 glomeruli from 6 mice (washout, n = 8). (C) Histogram showing analysis of the area under the curve (AUC) in percentage of the control value. Data represent mean (B, solid lines; C, boxes) ± SEM (B, dashed lines; C, error bars).

although this was difficult to determine due to spontaneous transients. Figure 4B (mouse #1) shows a frequently observed case in which the decrease in Ca^{2+} occurred after the onset of the RBC velocity increase, suggesting that Ca^{2+} signaling in thin-strand, juxta-synaptic pericytes does not trigger the onset of local functional hyperemia. This hypothesis was strengthened with experiments that tested how these pericytes responded to high concentrations of non-specific odors. Such odors were able to increase RBC velocity in the absence of a local synaptic activation and without affecting pericyte Ca^{2+} or Ca^{2+} transient frequency (Figures 4C and 4D). These results demonstrate that the Ca^{2+} decreases in thin-strand, juxta-synaptic pericytes were indeed caused by local synaptic activation but also indicated that the onset of the blood flow increase was driven by a more upstream site, consistent with results showing that global, but not local, blockade of synaptic transmission is required to fully block local functional hyperemia (Chaigneau et al., 2007) and that hemodynamic responses can occur in absence of local neuronal activation (Jukovskaya et al., 2011; O'Herron et al., 2016).

Upon averaging, a minor diameter increase appeared in juxta-synaptic capillaries (Figure 5). However, because this "dilation" was smaller than our microscope point spread function (xy plane), associated with a transient lateral movement (Figure S5), did not precede the local velocity increase, and occurred in response to odors that did not activate local synapses, we considered that, if not artifactual, it passively resulted from the increase in blood flow. Note that as capillaries underlie most of the vascular bed resistance (Blinder et al., 2013), such a passive dilation may strongly influence resting blood flow and functional hyperemia (see our modeling below).

Pericytes and SMCs Upstream of the Synapse Are "Synchronously" Activated but Mediate Distinct Local Hemodynamic Responses

To locate the upstream site of blood flow regulation and investigate the precise timing of hemodynamic changes along the entire vascular tree, we traced the direction of RBC flow from the juxta-synaptic capillary back to the feeding pial arteriole (Figure 5A). We found that the blood supply to dorsal glomeruli capillaries originated from vessels below the glomerulus that branched off of parenchymal arterioles (mean diameter of 10.2 ± 0.5 μm, n = 9) located in the mitral cell or external plexiform layers (vascular distance from juxta-synaptic capillary to upstream parenchymal arteriole: 402 ± 55 μm, n = 8). Upstream capillaries became larger in diameter (6.1 ± 0.3 μm, n = 18) and progressively enwrapped by pericytes whose morphology differed from the higher-order juxta-synaptic capillaries as previously described (Attwell et al., 2016; Burdyga and Borysova, 2014; Grant et al., 2017; Hill et al., 2015) (see examples in Figures S3 and S6 and Video S3). At the level of these larger enwrapped capillaries (first- to approximately fourth- to sixth-order capillaries) and the upstream parenchymal arteriole, we unexpectedly observed a rapid Ca^{2+} drop in response to odor that was synchronous in all enwrapping pericytes and arteriolar SMCs. The fast and synchronous Ca^{2+} drop is consistent with a back-propagating hyperpolarization along the endothelium (Chen et al., 2014; Longden et al., 2017), which our data suggest is transmitted to the upstream enwrapping pericytes in addition to SMCs. Surprisingly, these synchronized decreases in Ca^{2+} generated dilations with different dynamics along the vascular tree. The most rapid dilations were observed in both the parenchymal arteriole and the proximal part of the first-order capillary (less than ~50 μm from the arteriole) with indistinguishable onset (Figure 5B; Figures S6 and S7; Video S4). Dilations were also observed in more distal pericyte enwrapped capillaries (more than ~50 μm from the arteriole); however, these occurred with a delayed onset and rising phase. Paradoxically, the timing of RBC velocity increases in these compartments was reversed: RBC velocity increased fastest in the distal capillaries that dilated slowly and decreased or increased with a delay in the parenchymal arteriole and the proximal portion of the first-order capillary (Figure 5B; Figures S6 and S7). In summary, the first-order capillary dynamics were complex: in most cases (8/9), the proximal 50 μm portion of the capillary and the arteriole dilated simultaneously, and when more than ~50 μm downstream of

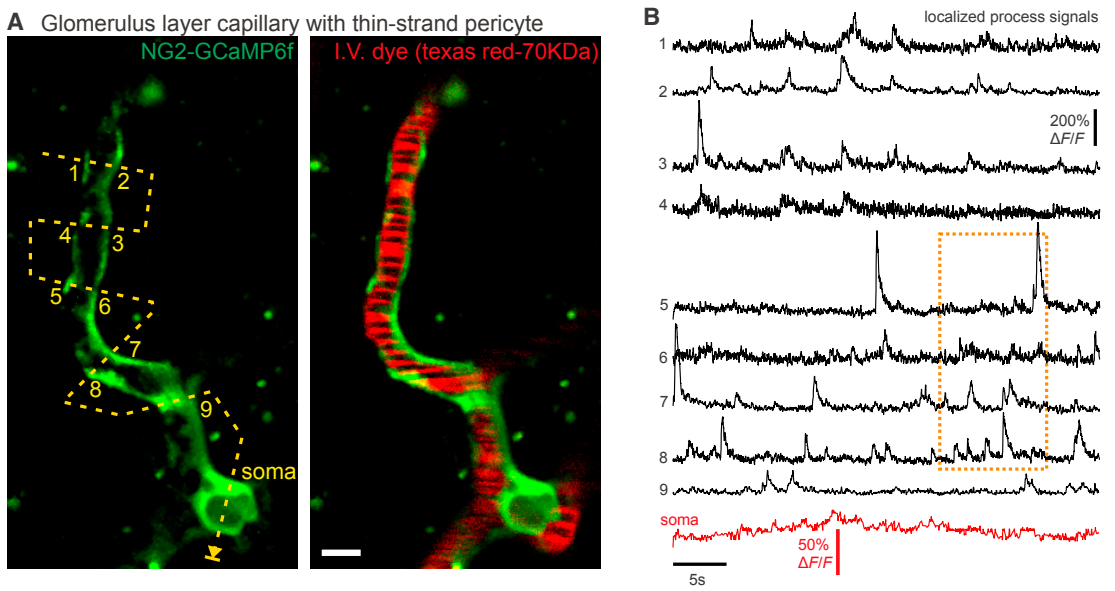

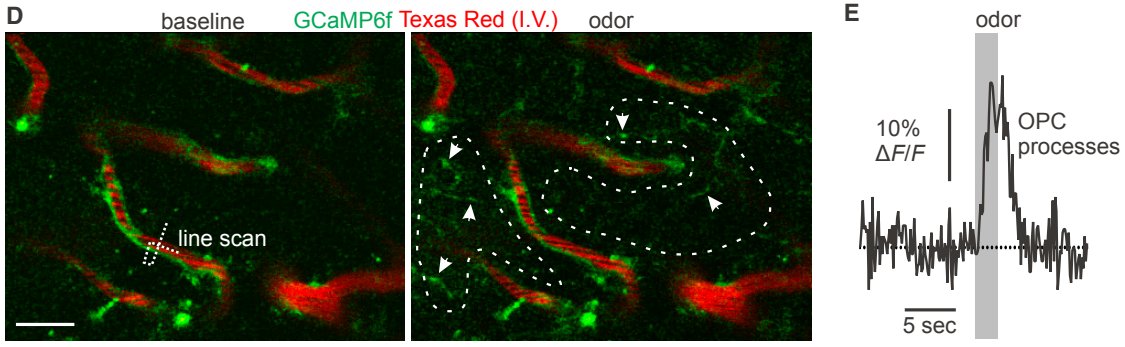

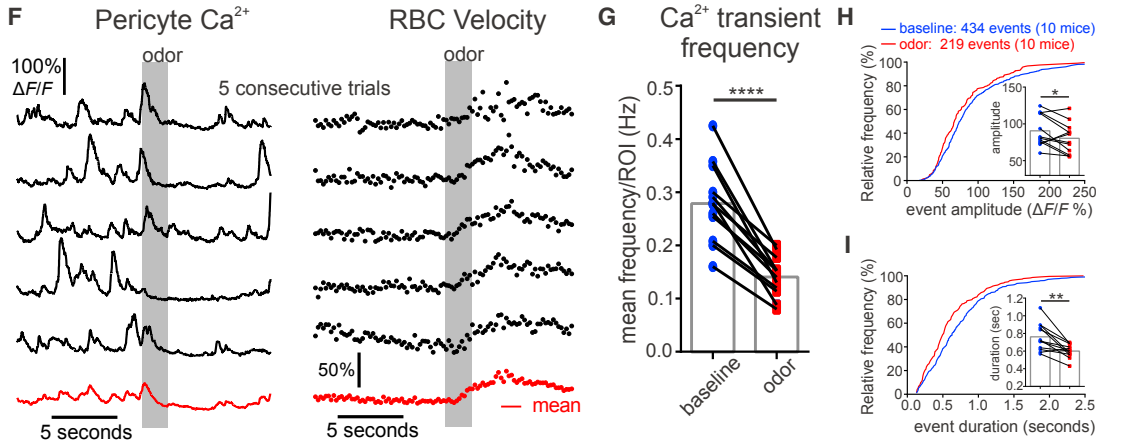

(legend on next page)

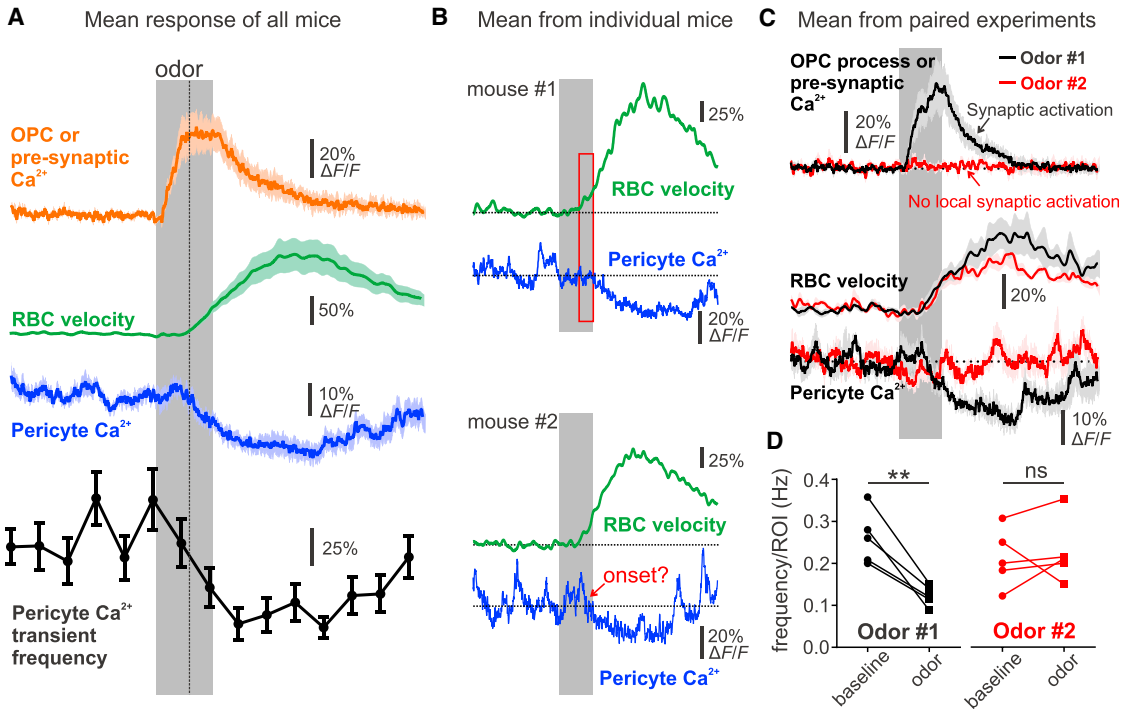

Figure 4. Decreases in Thin-Strand Pericyte Ca^{2+} Require Local Synaptic Activation

(A) Summarized traces (all mice). The vertical dashed line serves as a visual cue to indicate a similar onset between the mean pericyte Ca^{2+} decrease and RBC velocity increase. n = 12 glomerulus pericytes from 12 mice (including data from 5 glomeruli shown in C and D).

(B) Mean responses of pericyte Ca^{2+} and RBC velocity from two different mice. These two individual cases illustrate that RBC velocity can increase before the onset of the pericyte Ca^{2+} decrease or that this onset can be masked by spontaneous Ca^{2+} activity. Red box indicates estimated onset of the signals.

(C) Responses of synaptic input (either pre-synaptic Ca^{2+} or OPC process Ca^{2+}), RBC velocity, and longitudinal pericyte process Ca^{2+} to two different odors: one that locally activates neurons and one that does not. The odor (in red) that does not activate neurons does not affect steady-state Ca^{2+} or transients in pericytes; however, it increases the capillary RBC velocity, suggesting that RBC flow to the juxta-synaptic capillary is regulated at an upstream location.

(D) Summary graph of the role of local neuronal activation (odors #1 and #2) on pericyte Ca^{2+} transients, paired experiments from five mice.

Data in (A) and (C) represent mean ± SEM. See Figures 3, S4, and S5 and Videos S2 and S3.

the arteriole-capillary junction, the first-order branch behaved as higher-order capillaries (Figure S6, top), suggesting that these dynamics are not branch specific. Note that in a single case (1/9), the proximal portion dilated slowly as in higher-order capillaries and RBC velocity increased rapidly (Figure S7E). In a separate set of experiments, we then tested whether the fast Ca^{2+} decrease extended upstream to pial vessels, where dilation is known to be delayed (Chen et al., 2014; Tian et al., 2010). When comparing the onset of the Ca^{2+} drop in SMCs of pial vessels to paired downstream parenchymal arterioles that dilated

Figure 3. Thin-Strand Glomerulus Pericytes Sense Synaptic Activity via Decreases in Microdomain Ca^{2+} Transients

(A) Single z plane image shows GCaMP6f fluorescence (green) of a glomerulus layer thin-strand capillary pericyte (branch order 7). Dashed line indicates path of broken line scan with ROIs numbered (1–9). Scale bar, 5 μm.

(B) Δ*F*/*F* measurements of spontaneous activity in different ROIs show frequent calcium transients that are mostly independent of signals in other ROIs and the soma.

(C) Portion of total line scan shown in (A) (ROIs 5–8, 10 s). Scale bar, 5 μm.

(D) Left: image shows longitudinal processes of glomerular pericytes expressing GCaMP6f along capillaries labeled with Texas red dextran (70 kDa). The broken line indicates the process and capillary simultaneously monitored in (F). Right: upon odor inhalation, Ca^{2+} rises in OPC processes, which appear in the glomerular neuropil (see arrows).

(E) The single trial OPC Ca^{2+} response, measured within the ROIs outlined (dashed white line) in (D), is taken as a marker of neuronal activation.

(F) Left: activation of the glomerulus is followed by a decrease in the frequency of pericyte process Ca^{2+} transients and the steady-state Ca^{2+} concentration (average of two ROIs crossing the pericyte process). Right: RBC velocity increases in the capillary. Black traces show individual trials, and the red trace shows mean of five trials. Note: the apparent increase in Ca^{2+} that occurs prior to the decrease is due to the high frequency of spontaneous events as it begins to rise before the onset of the odor stimulation and is not apparent in the average across mice shown in Figure 4.

(G) Summarized plots of pericyte process Ca^{2+} transient frequency 5 s before and after the onset of the odor stimulation.

(H and I) Cumulative frequency histograms and mean values (insets) of pericyte process Ca^{2+} transient amplitude (H) and duration (I) 5 s before and after the onset of the odor stimulation. Data represent mean ± SEM.

See Figures 4, S3, S4, and S5 and Videos S2 and S3.

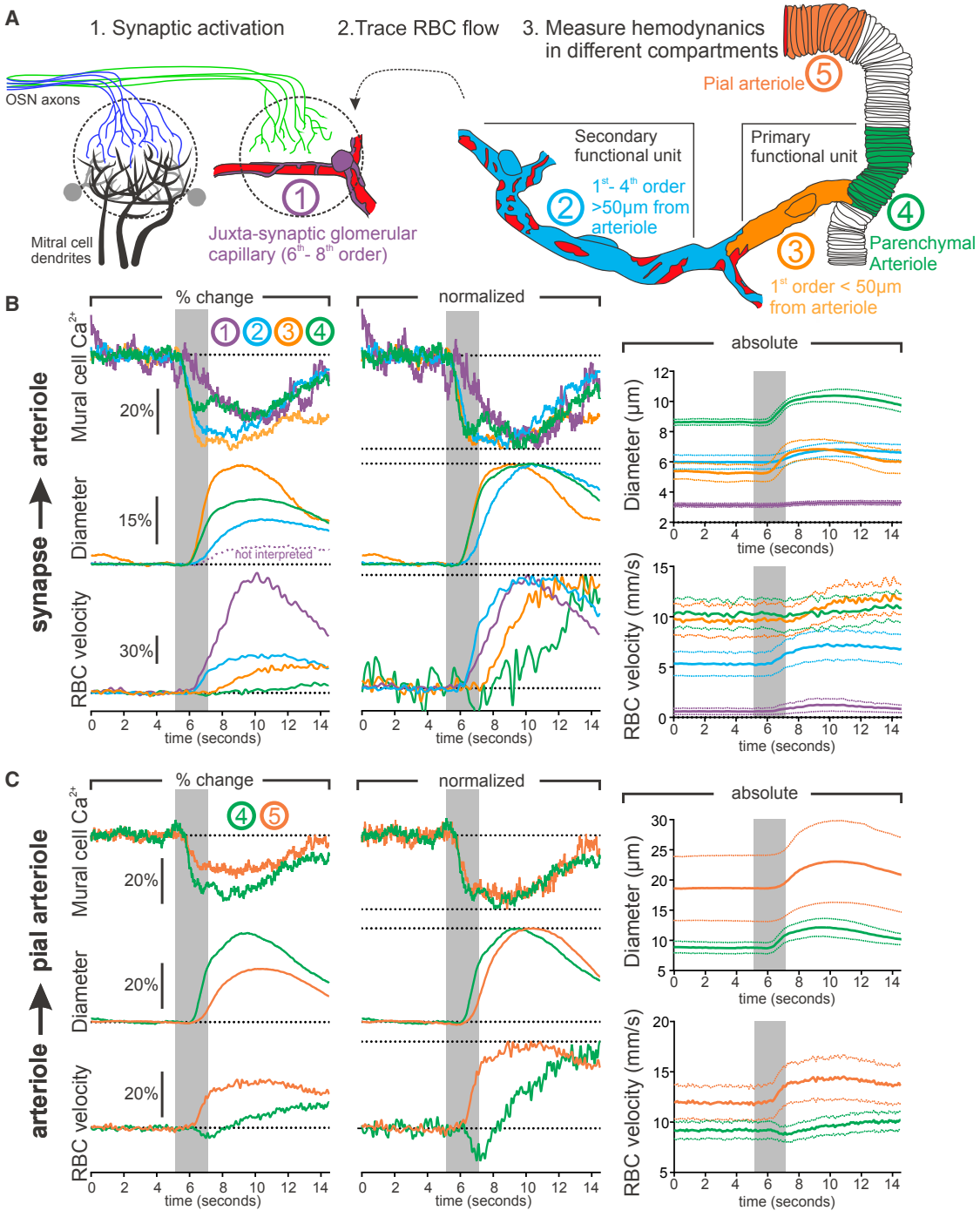

Figure 5. The Timing of Functional Hyperemia from the Synapse to the Pia

(A) Schematic of experimental design. First, glomerular capillaries with thin-strand-type pericytes are imaged adjacent to recorded synaptic activation. Second, the direction of blood flow is traced backward to the upstream arteriole. Third, vessel diameter and RBC velocity are measured in different vascular compartments.

(B) Paired recordings displaying the average timing of the decrease in mural cell Ca^{2+} (top), vessel diameter (middle), and RBC velocity in different vascular compartments upstream of the juxta-synaptic capillary. Dashed purple line indicates the quantified fluorescent lumen diameter in glomerulus capillaries, which was not interpreted. Left: mean responses; middle; normalized data; right: absolute values (4 vascular networks, 3 mice).

(C) Paired recordings displaying the average timing of the decrease in SMC Ca^{2+} (top), vessel diameter (middle), and RBC velocity in a parenchymal arteriole (100–230 µm deep) compared to its upstream feeding pial vessel. Left: mean responses; middle: normalized data; right: absolute values (5 vessel pairs, 3 mice). See Figures S6 and S7 and Video S4.

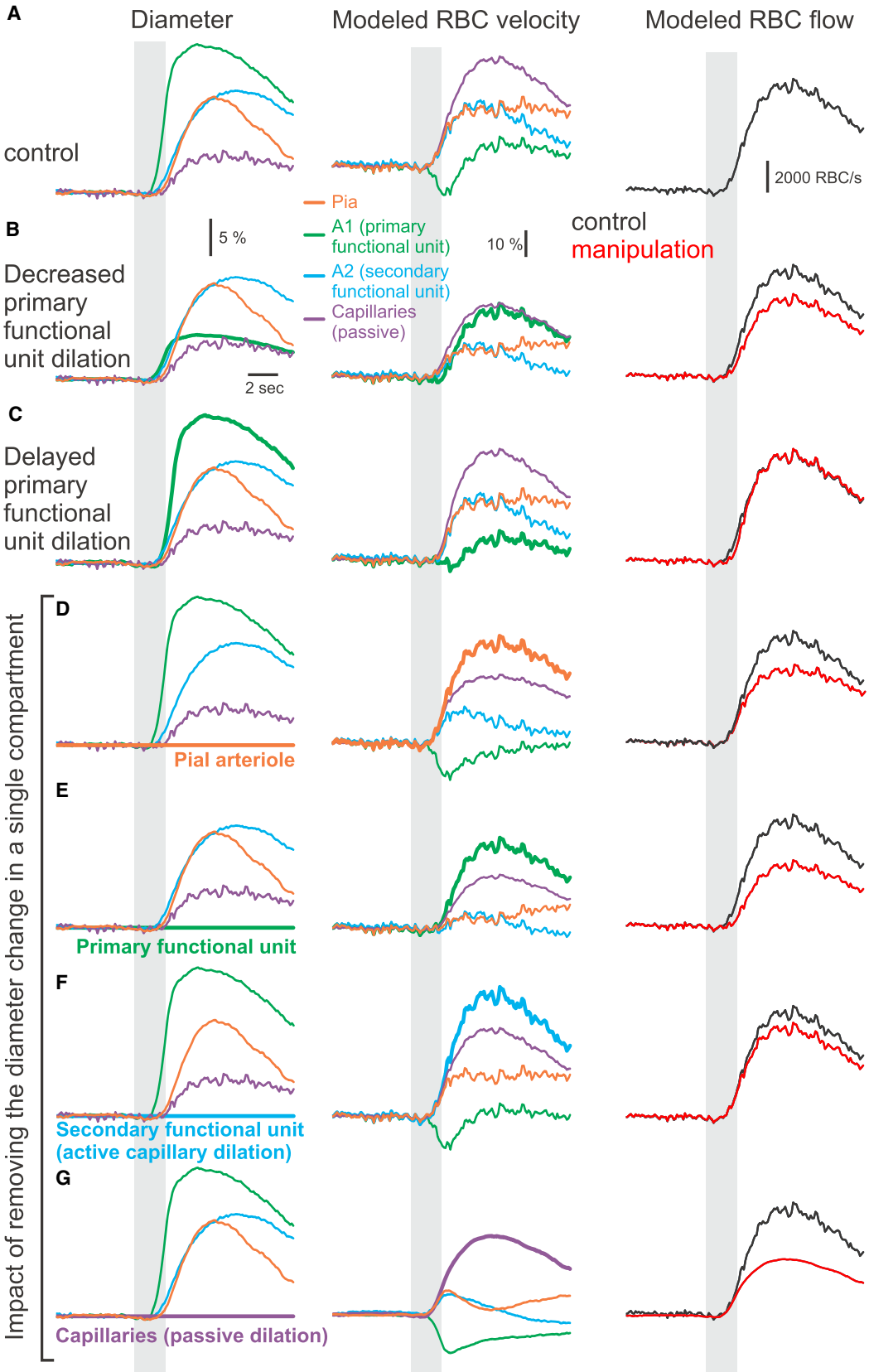

(legend on next page)

fast, no detectable difference in the onset of the Ca^{2+} drop was observed despite the fact that these pial vessels consistently dilated slower (Figure 5C). Normalized plots show that despite the delay in the pial arteriole dilation, the RBC velocity changes occurred as rapidly as in vessels downstream of the parenchymal arteriole and the proximal part of the first-order capillary. These results demonstrate that synaptic activity generates a synchronous Ca^{2+} drop in pericytes and SMCs along the entire upstream vascular tree. These Ca^{2+} drops result in vessel dilations with differential dynamics that can be used to categorize the vasculature into two functional units: a primary unit comprising the parenchymal arteriole and its first-order capillary and a secondary unit comprising downstream (second- to sixth-order capillaries) vessels. The onset of functional hyperemia is driven by the primary unit, characterized by a rapid dilation and increase in blood volume but a paradoxical decrease or delayed increase of blood velocity. In the secondary unit, the dilation is slower and lags a fast velocity increase, which is rapidly transmitted to downstream capillaries, with the largest proportional velocity increase occurring in the juxta-synaptic capillaries (Figure 5B). However, although the pericytes of the secondary unit dilate slower, they may actively function to increase the proportion of the blood flow increase that reaches the activated synapses (see below).

Modeling Compartmentalized RBC Velocity Dynamics in Response to Vessel Diameter Changes

Our experimental data on compartmentalized hemodynamics led us to further investigate whether RBC velocity changes could be predicted with mathematical modeling. We therefore designed a simplified four-compartment vascular model and calculated RBC flow and velocity in each compartment as a function of the diameter of every compartment (Figure 6A; see Data S1). The compartments were divided as follows: Pia, pial arterioles; A1, the primary functional unit (parenchymal arteriole and fast-dilating first-order capillary); A2, more slowly dilating enwrapped approximately second- to fifth-order capillaries; and Capillaries, passively dilating capillaries (from the activated glomerulus until the junction with the secondary unit). Blood flow was conserved from one compartment to another. In response to the median experimental diameter measurements obtained from paired recordings across compartments, the model predicted differential RBC velocity dynamics in the compartments that were in line with the experimental results: a decrease and delayed increase in velocity in the primary functional unit (A1), with a simultaneous increase in velocity within the downstream and upstream compartments (pia, A2, glomerular capillaries) and the largest proportional increase occurring in the juxta-synaptic capillaries (Figure 6A). The model was robust, and the general dynamics were not affected by ±10% changes of resting capillary divergence or viscosity. Furthermore, it allowed us to manipulate the inputted diameter changes and test their impact on the resulting velocity and flow changes. In A1, limiting the diameter change amplitude to 30% of the control value removed the local transient velocity drop, revealing a large, delayed velocity increase and a reduction of the velocity increase in the three other compartments (Figure 6B). Note that it also decreased the change in blood flow. Alternatively, removing the delay between the dilation of the primary unit and the other compartments decreased the magnitude of the initial velocity drop (Figure 6C). Figures 6D–6G show the impact of completely removing the diameter change within each of the separate compartments. Blockade of the dilation in any single compartment affected the hemodynamics in other compartments. Blockade of the A2 (secondary functional unit) dilation decreased the blood flow change, demonstrating that active capillary dilation participates in functional hyperemia. Strikingly, blockage of the passive capillary dilation dramatically affected the hemodynamic response in the other compartments as well as the blood flow change. This stresses that in the olfactory bulb as in the cortex, most of the vascular bed resistance comes from small capillaries (Blinder et al., 2013), and therefore, even small, passive changes to the diameter of these capillaries are expected to greatly facilitate the increase in blood flow. Our modeling faithfully illustrates that compartmentalized RBC velocity dynamics results from the timing and relative changes of diameter that occur in the different vascular compartments.

Vascular Compartmentalization of Hemodynamics in Awake Head-Fixed Mice

As anesthetics affect both neuronal activity and neurovascular coupling mechanisms (Masamoto and Kanno, 2012), in a final set of experiments, we tested whether compartmentalized hemodynamics follow similar rules in awake mice. Due to slight motions in awake mice, we decided not to attempt to measure capillary diameter changes or pericyte Ca^{2+} responses but instead to focus on measurements of RBC velocity changes in the different vascular compartments and their relation to the upstream arteriole dilation. We first habituated awake Thy1-GCaMP6f (GP5.11) mice to our experimental setup and mapped responsive glomeruli. As previously shown in anesthetized mice

Figure 6. Modeling Compartmentalized RBC Velocity Dynamics in Response to Vessel Diameter

(A–G) Left: diameter changes (normalized) in response to odor stimulation in pia (pial arteriole, brown), A1 (primary functional unit, green), A2 (secondary functional unit, blue), and capillaries (small passively dilating capillaries, purple). Middle: modeled velocity in response to the experimental diameter response. Right: modeled blood flow in the same conditions (red: response to diameter changes from the left panel, black: control conditions from A).

(A) Median paired experimental response to odor stimulation.

(B) Same as (A) except that the A1 diameter change was decreased by 70%.

(C) Same as (A) except that the A1 diameter was delayed to match onset of other compartments

(D–G) Same as (A) except that the diameter change is abolished in either the pial arteriole (D), the primary functional unit (E), the secondary functional unit (F), or the passively dilating capillaries (G), while the diameter change in the other three compartments was not modified. This diameter change abolition in a given compartment increases the velocity response in the same compartment as long as it actively dilates upon odor. In contrast, in the passive glomerular capillary compartment, the velocity response is smaller than control when the diameter remains constant (i.e., the compartment resistance remains constant and, therefore, the blood flow change is significantly smaller). Note that the decrease in noise is caused by the absence of fluctuations in the capillary diameter response. Gray bars indicate timing of odor application.

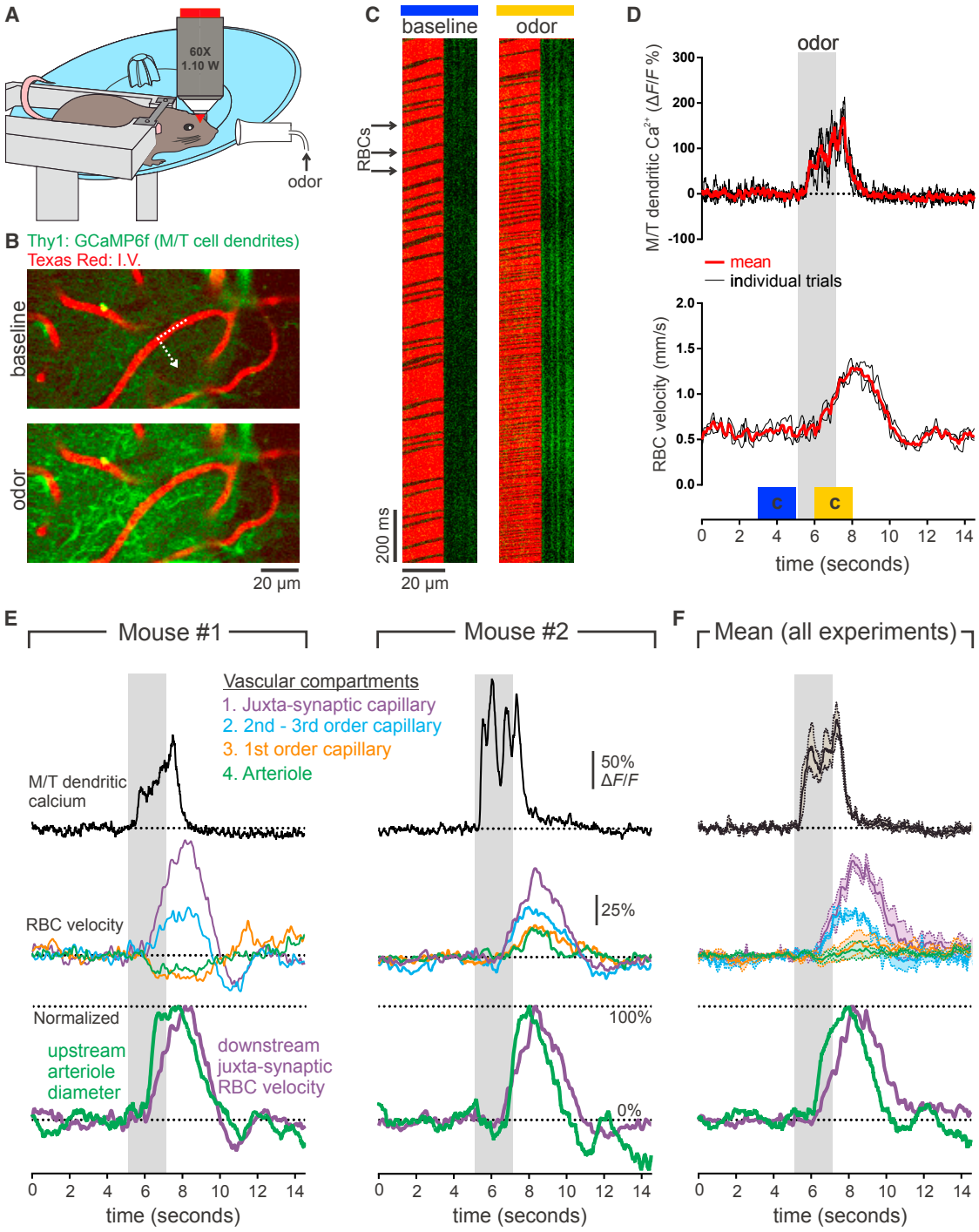

Figure 7. Compartmentalized Hemodynamics in Awake Mice

(A) Schematic of the experimental setup: head-fixed mouse on running wheel was trained to stay still during odor application while imaging olfactory bulb via a chronic cranial window.

(B) Glomerular activation was first mapped by recording Ca^{2+} elevations in the mitral and tufted cell dendritic tufts of Thy1:GCaMP6f mice.

(C) Example images from the broken line scan through the capillary and into the neuropil show that odor evokes an increase in M/T cell Ca^{2+} (green) and an increase in RBC velocity (shadows in the red channel).

(D) Quantification of experiment illustrated in (B) and (C) showing three consecutive trials evoking reproducible neuronal and RBC velocity responses. Blue and yellow blocks indicate time period shown in (C).

(legend continued on next page)

(Rungta et al., 2017), presentation of odor resulted in reproducible Ca^{2+} increases in the tuft of mitral/tufted cells, followed by an increase in glomerular capillary RBC velocity (Figures 7A–7D). Following tracing of blood flow to the feeding arteriole, recordings of RBC velocity in different upstream compartments were made. As observed in anesthetized mice, in awake mice, both decreases (Figure 7E, mouse #1) and delayed increases (Figure 7E, mouse #2) in blood velocity were observed in the parenchymal arteriole as well as in the first-order capillary, whereas blood velocity increased rapidly in second- and third-order capillaries with proportionally the largest increase in RBC velocity occurring in the juxta-synaptic capillary (Figures 7E and 7F). Finally, normalized measurements of arteriole diameter and juxta-synaptic RBC velocity show that the arteriole dilation precedes the downstream increase in velocity at the site of synaptic input (Figures 7E and 7F).

DISCUSSION

The main purpose of our study was to examine the functional roles of the mural cells located on arterioles versus capillaries and not to add to the controversy that exists regarding whether pericytes can actively dilate, which is largely due to the existence of different types of pericytes and differences in naming the cells that enwrap capillaries closer to the arteriole (Attwell et al., 2016; Grant et al., 2017; Hill et al., 2015). We classified the vessels that penetrated downward from the pia surface toward the mitral cell layer and that were surrounded by a continuous layer of SMCs as parenchymal arterioles. The vessels that branched off these arterioles and were immediately associated with a transition to smaller sizes and the passage of RBCs in single file were called capillaries and were numbered according to their branching order. Cre-dependent expression of GCaMP6f under the NG2 promoter allowed us to image the dynamics of Ca^{2+} signaling in all types of mural cells from the thin-strand pericytes in higher-order capillaries to the upstream SMCs enwrapping pial arterioles. The high sensitivity and fast kinetics of GCaMP6f revealed that all pericytes are dynamic at rest, with frequent microdomain Ca^{2+} elevations within their processes. Although the purpose of these spontaneous Ca^{2+} transients remains unknown, our results suggest that they partially set the resting Ca^{2+} level of pericytes, as their decreases in frequency upon odor is associated with a drop in baseline fluorescence.

Up until now, the thin-strand-type pericytes have largely been suggested as passive cells (Hill et al., 2015); however, the use of GCaMP6f definitively demonstrates that they respond to synaptic activation. Interestingly, their activation does not trigger the onset of functional hyperemia, which often precedes the Ca^{2+} drop in thin-strand processes. Therefore, although the function of this delayed Ca^{2+} drop remains unclear, an intriguing possibility would be that this pericyte activation increases the capillary elasticity and facilitates their passive dilation. The finding that the upstream enwrapping-type pericytes on larger capillaries display Ca^{2+} drops before the thin-strand juxta-synaptic pericytes is quite surprising as these thin-strand pericytes are located in the immediate vicinity of the glomerular synaptic input and would be expected to exhibit the fastest drop in Ca^{2+}. We believe that the onset of the Ca^{2+} decreases in upstream enwrapping-type pericytes and SMCs is triggered by a rapid retrograde hyperpolarization along the endothelium (Longden et al., 2017), which could then be transmitted to the mural cells via myo-endothelial gap junctions (Figueroa and Duling, 2009; Haddock et al., 2006; Zhang et al., 2014). Several mechanisms could underlie the hyperpolarization-induced Ca^{2+} decrease, such as a shift in a window current or a decrease in Ca^{2+} transients due to closure of voltage-dependent calcium channels (Longden et al., 2016; Tykocki et al., 2017), which would reduce global intracellular Ca^{2+} and trigger vasodilation. As the expression profile of both pericytes and endothelial cells changes along the artery-capillary-venous axis (e.g., Vanlandewijck et al., 2018), one possibility for the timing difference between Ca^{2+} decreases in thin-strand (juxta-synaptic) versus more upstream enwrapping-type pericytes is that different pericyte subtypes along the artery-capillary-venous axis are differentially gap-junctionally coupled to the endothelium. Whether the Ca^{2+} drop in thin-strand pericytes results from decreased endothelial-pericyte coupling or from other signaling mechanisms, such as the local release of prostaglandins from astrocytes acting directly on pericytes (Mishra et al., 2016), remains an intriguing question. Note that our control experiments based on a spectral shift in the Ca^{2+} sensitivity of GCaMP6f validate that these Ca^{2+} changes are not caused by movement or shape changes (Figure S4), and as GCaMP variants are becoming a common tool in neuroscience, we propose using this as a common and easy to implement control when volume changes or small movements are of concern. Further to this control, experiments in which blood flow was increased with non-specific odors that did not increase local synaptic activation were not associated with a change in thin-strand pericyte Ca^{2+} levels.

The synchronous nature of our Ca^{2+} drops in the upstream mesh-type pericytes and SMCs is consistent with a fast back-propagating voltage signal (Chen et al., 2014; Emerson and Segal, 2000; Iadecola et al., 1997; Longden et al., 2017) in which the extremely small timing differences between compartments would not be detectable with our Ca^{2+} imaging approach and therefore appear ''synchronous.'' Furthermore, the fact that synchronous mural cell activation was associated with distinct differences in the timing of vessel dilation implies that mural cell activation is a more accurate temporal marker (with a delay) of synaptic activation than vessel diameter, which varies according to the vascular compartment. The timing of the primary unit (arteriole and first-order) dilation (~600–700 ms delay from the onset of synaptic activation) is in line with the timing of arteriole dilations measured with two-photon microscopy in deeper layers of the

(E and F) Hemodynamics in different vascular compartments in response to downstream synaptic activation. Top: M/T dendritic Ca^{2+} shows glomerular activation; middle: RBC velocity changes in different vascular compartments; bottom: normalized values of arteriole diameter and RBC velocity changes in the downstream juxta-synaptic capillary. (E) Recordings from individual mice show an example in which velocity decreases in the primary functional unit (arteriole and first-order capillary) but increases rapidly in all downstream capillaries (left) and an example in which the primary functional unit shows a delayed increase in velocity (right). (F) Mean of all experiments (4 olfactory bulbs from 3 mice). Data represent mean (solid line) ± SEM (dotted line).

cortex (Tian et al., 2010; Uhlirova et al., 2016) and the onset of single vessel CBV-fMRI signals in midcortical layers (Yu et al., 2016). Furthermore, the onset of our upstream mural cell Ca^{2+} drop (~300 ms) is almost identical to the reported onset time of the upstream SMC hyperpolarization in response to stimulation of capillaries with potassium in an isolated cortical capillary-arteriole *in vitro* preparation (Longden et al., 2017). In contrast, some groups have also reported capillary dilation in advance of arterioles in the cortex (Hall et al., 2014; Kisler et al., 2017; Mishra et al., 2016). Although this may be explained by differences in the anesthesia used or by the fact that the imaged vessels were not traced back from the activated synapses, we cannot discard the possibility that regional differences may exist in the types of mural cells present along the vascular arbor.

The strength of our study lies in the precise description of the Ca^{2+} dynamics in mural cells surrounding different vascular compartments and addressing how these signals correlate with the corresponding compartmentalized hemodynamics along the vascular arbor upstream of the precise site of synaptic input. Based on our data, we believe that functional hyperemia starts at the level of the primary unit. There, the rapid increase in the cross-sectional area of the vessel causes a drop in resistance and generates a blood flow increase despite the initial delay or decrease in velocity that occurs locally. As blood flow is conserved, RBC velocity increases rapidly in the upstream pia and the downstream capillaries that dilate slowly. One previous study reported that RBC velocity increases in capillaries before arterioles (Wei et al., 2016), and the authors attributed this difference to a local decrease of oxygenation and a subsequent change of RBC morphology facilitating the flow. Although oxygen-dependent RBC morphology changes may occur, they cannot be responsible for the onset of functional hyperemia as the upstream primary unit dilation always precedes the capillary RBC velocity increase. In support of our experimental conclusions, we show that inputting the experimentally recorded compartmentalized diameter changes into a four-compartment model well predicts RBC velocity changes similar to the experimental values. The strength of the model is to show how the relative magnitude of the dilations in different compartments affect the hemodynamics in different compartments. The model also highlights how the minor and passive diameter changes of juxta-synaptic capillaries have a large impact on the resulting hemodynamics. Although small and difficult to interpret from our experimental data, these passive dilations are required by the model to explain our experimentally obtained velocity measurements. The model also reveals that both the primary unit and the secondary unit, which are most probably covered by different types of SMCs and pericytes, contribute to functional hyperemia. However, we acknowledge that our model may not perfectly reflect reality as it assumes that within each vascular compartment, all the vessels dilate homogeneously. It should also be noted that the impact of the primary and secondary unit dilations on blood flow is, in reality, larger than what is presented by abolishing them in our model (Figures 6D and 6E) as the increase in flow driven by these dilations drives the passive dilation of downstream capillaries, which was left intact in the model. Although, the specific mechanisms underlying the differential kinetics of the Ca^{2+} drops and the dilation of the contractile mural cells in each vascular compartment remain to be established, our experimental and modeling data suggest that the unique temporal dynamics of velocity, volume, and flow changes in combination with their proportional increases could be used to improve the interpretation of hemodynamic-based functional imaging.

A secondary and serendipitous finding of our work is that OPCs respond to OSN terminal activation via fast and odor-specific Ca^{2+} elevations in their processes. Since the first demonstration of glutamatergic synapses on hippocampal OPCs (Bergles et al., 2000), it is now established from numerous *in vitro* studies that these cells respond to neuronal activation via various different mechanisms in several brain regions (for review, see Maldonado and Angulo, 2015). However, the demonstration of their activation *in vivo* was previously hampered by the non-specificity of conventional bulk dye loading techniques, a limitation which is overcome in NG2cre;GCaMP6f mice as OPCs were easily distinguishable from pericytes and SMCs. We show, for the first time, neuronal input-specific OPC Ca^{2+} elevations *in vivo*. These OPC process Ca^{2+} elevations display matching odorant selectivity as the OSN terminal activation. The OPC process Ca^{2+} elevations are biphasic with extremely rapid initial elevations detectable in a subset of processes and with secondary slower Ca^{2+} events occurring in the same and other processes that sometimes invade the periglomerular OPC somata, in particular, upon stronger stimulation. In glomeruli that contained processes from OPCs expressing GCaMP6f, a neuronal signal (OSN terminals) was always followed by a ''fast'' OPC signal within the activated glomerulus, demonstrating that these signals can be used as reliable temporal and spatial markers of glomerular activation. Using a natural odor stimulation in which the OSN terminals are not activated synchronously but only gradually even within a single sniff, we were unable to accurately detect the delay between the input (OSNs) and the initial output (OPCs) signals. To separate OSN terminal and OPC responses with accurate temporal precision would likely require targeting a bipolar electrode onto an OSN axon fascicule converging into a glomerulus in order to synchronously activate the axons. Such an approach should permit accurate distinction between the timing of monosynaptic, polysynaptic, or extrasynaptic OPC activation. *In vivo* pharmacology indicates that the OPC Ca^{2+} elevation depends on the local release of glutamate. However, whether these signals occur via direct glutamatergic activation of OPCs, synaptic or di-synaptic release of a secondary transmitter, or even possibly a secondary interaction with another cell type remain unknown. In summary, although OPC process Ca^{2+} elevations serve as reliable markers of synaptic input in the olfactory bulb glomerulus, our observations also highlight the complexity of these Ca^{2+} signals and set the stage for future work on identifying the precise mechanisms underlying activity-dependent OPC Ca^{2+} signals.

STAR★METHODS

Detailed methods are provided in the online version of this paper and include the following:

- KEY RESOURCES TABLE
- CONTACT FOR REAGENT AND RESOURCE SHARING

SUPPLEMENTAL INFORMATION

Supplemental Information includes four figures, five videos, and two data files and can be found with this article online at https://doi.org/10.1016/j.neuron.2018.06.012.

ACKNOWLEDGMENTS

We thank Axel Pries for comments on an earlier version of the manuscript. We thank Y. Goulam-Houssen for technical support. Financial support was provided by the Institut National de la Santé et de la Recherche Médicale (INSERM), the European Research Council (ERC-2013-AD6; 339513), the Agence Nationale de la Recherche (ANR/NSF 15-NEUC-0003-02 and NR-16-RHUS-0004 [RHU TRT_cSVD]), and the Fondation Leducq Transatlantic Networks of Excellence program (16CVD05, Understanding the role of the perivascular space in cerebral small vessel disease). R.L.R. had a postdoctoral fellowship award from EMBO (ALTF 384-2015).

AUTHOR CONTRIBUTIONS

R.L.R. and S.C. designed the study, interpreted the data, and wrote the paper. R.L.R. performed and analyzed all experiments. E.C. performed modeling and edited the paper. B.-F.O. wrote the velocity analysis software.

DECLARATION OF INTERESTS

The authors declare no competing interests.

Received: November 14, 2017
Revised: March 29, 2018
Accepted: June 7, 2018
Published: June 21, 2018

SUPPORTING CITATIONS

The following reference appears in the Supplemental Information: Autio et al. (2011).

REFERENCES

Attwell, D., Mishra, A., Hall, C.N., O'Farrell, F.M., and Dalkara, T. (2016). What is a pericyte? J. Cereb. Blood Flow Metab. *36*, 451–455.

Autio, J., Kawaguchi, H., Saito, S., Aoki, I., Obata, T., Masamoto, K., and Kanno, I. (2011). Spatial frequency-based analysis of mean red blood cell speed in single microvessels: investigation of microvascular perfusion in rat cerebral cortex. PLoS ONE *6*, e24056.

Bergles, D.E., Roberts, J.D., Somogyi, P., and Jahr, C.E. (2000). Glutamatergic synapses on oligodendrocyte precursor cells in the hippocampus. Nature *405*, 187–191.

Biesecker, K.R., Srienc, A.I., Shimoda, A.M., Agarwal, A., Bergles, D.E., Kofuji, P., and Newman, E.A. (2016). Glial cell calcium signaling mediates capillary regulation of blood flow in the retina. J. Neurosci. *36*, 9435–9445.

Blinder, P., Tsai, P.S., Kaufhold, J.P., Knutsen, P.M., Suhl, H., and Kleinfeld, D. (2013). The cortical angiome: an interconnected vascular network with noncolumnar patterns of blood flow. Nat. Neurosci. *16*, 889–897.

Burdyga, T., and Borysova, L. (2014). Calcium signalling in pericytes. J. Vasc. Res. *51*, 190–199.

Chaigneau, E., Tiret, P., Lecoq, J., Ducros, M., Knöpfel, T., and Charpak, S. (2007). The relationship between blood flow and neuronal activity in the rodent olfactory bulb. J. Neurosci. *27*, 6452–6460.

Chen, B.R., Kozberg, M.G., Bouchard, M.B., Shaik, M.A., and Hillman, E.M. (2014). A critical role for the vascular endothelium in functional neurovascular coupling in the brain. J. Am. Heart Assoc. *3*, e000787.

Collot, M., Wilms, C.D., Bentkhayet, A., Marcaggi, P., Couchman, K., Charpak, S., Dieudonné, S., Häusser, M., Feltz, A., and Mallet, J.-M.M. (2015). CaRuby-Nano: a novel high affinity calcium probe for dual color imaging. eLife *4*, 4.

Emerson, G.G., and Segal, S.S. (2000). Endothelial cell pathway for conduction of hyperpolarization and vasodilation along hamster feed artery. Circ. Res. *86*, 94–100.

Fernández-Klett, F., Offenhauser, N., Dirnagl, U., Priller, J., and Lindauer, U. (2010). Pericytes in capillaries are contractile in vivo, but arterioles mediate functional hyperemia in the mouse brain. Proc. Natl. Acad. Sci. USA *107*, 22290–22295.

Figueroa, X.F., and Duling, B.R. (2009). Gap junctions in the control of vascular function. Antioxid. Redox Signal. *11*, 251–266.

Grant, R.I., Hartmann, D.A., Underly, R.G., Berthiaume, A.-A.A., Bhat, N.R., and Shih, A.Y. (2017). Organizational hierarchy and structural diversity of microvascular pericytes in adult mouse cortex. J. Cereb. Blood Flow Metab. Published online January 1, 2017. https://doi.org/10.1177/0271678X17732229.

Haddock, R.E., Grayson, T.H., Brackenbury, T.D., Meaney, K.R., Neylon, C.B., Sandow, S.L., and Hill, C.E. (2006). Endothelial coordination of cerebral vasomotion via myoendothelial gap junctions containing connexins 37 and 40. Am. J. Physiol. Heart Circ. Physiol. *291*, H2047–H2056.

Hall, C.N., Reynell, C., Gesslein, B., Hamilton, N.B., Mishra, A., Sutherland, B.A., O'Farrell, F.M., Buchan, A.M., Lauritzen, M., and Attwell, D. (2014). Capillary pericytes regulate cerebral blood flow in health and disease. Nature *508*, 55–60.

Hill, R.A., Tong, L., Yuan, P., Murikinati, S., Gupta, S., and Grutzendler, J. (2015). Regional blood flow in the normal and ischemic brain is controlled by arteriolar smooth muscle cell contractility and not by capillary pericytes. Neuron *87*, 95–110.

Huang, W., Zhao, N., Bai, X., Karram, K., Trotter, J., Goebbels, S., Scheller, A., and Kirchhoff, F. (2014). Novel NG2-CreERT2 knock-in mice demonstrate heterogeneous differentiation potential of NG2 glia during development. Glia *62*, 896–913.

Iadecola, C. (2017). The neurovascular unit coming of age: a journey through neurovascular coupling in health and disease. Neuron *96*, 17–42.

Iadecola, C., Yang, G., Ebner, T.J., and Chen, G. (1997). Local and propagated vascular responses evoked by focal synaptic activity in cerebellar cortex. J. Neurophysiol. *78*, 651–659.

Jabs, R., Pivneva, T., Hüttmann, K., Wyczynski, A., Nolte, C., Kettenmann, H., and Steinhäuser, C. (2005). Synaptic transmission onto hippocampal glial cells with hGFAP promoter activity. J. Cell Sci. *118*, 3791–3803.

Jukovskaya, N., Tiret, P., Lecoq, J., and Charpak, S. (2011). What does local functional hyperemia tell about local neuronal activation? J. Neurosci. *31*, 1579–1582.

Kisler, K., Nelson, A.R., Rege, S.V., Ramanathan, A., Wang, Y., Ahuja, A., Lazic, D., Tsai, P.S., Zhao, Z., Zhou, Y., et al. (2017). Pericyte degeneration leads to neurovascular uncoupling and limits oxygen supply to brain. Nat. Neurosci. *20*, 406–416.

Kornfield, T.E., and Newman, E.A. (2014). Regulation of blood flow in the retinal trilaminar vascular network. J. Neurosci. *34*, 11504–11513.

Krogh, A., Harrop, G.A., and Rehberg, P.B. (1922). Studies on the physiology of capillaries: III. The innervation of the blood vessels in the hind legs of the frog. J. Physiol. *56*, 179–189.

Lecoq, J., Tiret, P., Najac, M., Shepherd, G.M., Greer, C.A., and Charpak, S. (2009). Odor-evoked oxygen consumption by action potential and synaptic transmission in the olfactory bulb. J. Neurosci. *29*, 1424–1433.

Lin, S., and Bergles, D. (2004). Synaptic signaling between GABAergic interneurons and oligodendrocyte precursor cells in the hippocampus. Nat. Neurosci. *7*, 24–32.

Longden, T.A., Hill-Eubanks, D.C., and Nelson, M.T. (2016). Ion channel networks in the control of cerebral blood flow. J. Cereb. Blood Flow Metab. *36*, 492–512.

Longden, T.A., Dabertrand, F., Koide, M., Gonzales, A.L., Tykocki, N.R., Brayden, J.E., Hill-Eubanks, D., and Nelson, M.T. (2017). Capillary K^+-sensing initiates retrograde hyperpolarization to increase local cerebral blood flow. Nat. Neurosci. *20*, 717–726.

Madisen, L., Garner, A.R., Shimaoka, D., Chuong, A.S., Klapoetke, N.C., Li, L., van der Bourg, A., Niino, Y., Egolf, L., Monetti, C., et al. (2015). Transgenic mice for intersectional targeting of neural sensors and effectors with high specificity and performance. Neuron *85*, 942–958.

Maldonado, P.P., and Angulo, M.C.C. (2015). Multiple modes of communication between neurons and oligodendrocyte precursor cells. Neuroscientist *21*, 266–276.

Masamoto, K., and Kanno, I. (2012). Anesthesia and the quantitative evaluation of neurovascular coupling. J. Cereb. Blood Flow Metab. *32*, 1233–1247.

Mishra, A., Reynolds, J.P., Chen, Y., Gourine, A.V., Rusakov, D.A., and Attwell, D. (2016). Astrocytes mediate neurovascular signaling to capillary pericytes but not to arterioles. Nat. Neurosci. *19*, 1619–1627.

O'Herron, P., Chhatbar, P.Y., Levy, M., Shen, Z., Schramm, A.E., Lu, Z., and Kara, P. (2016). Neural correlates of single-vessel haemodynamic responses in vivo. Nature *534*, 378–382.

Otsu, Y., Couchman, K., Lyons, D.G., Collot, M., Agarwal, A., Mallet, J.-M.M., Pfrieger, F.W., Bergles, D.E., and Charpak, S. (2015). Calcium dynamics in astrocyte processes during neurovascular coupling. Nat. Neurosci. *18*, 210–218.

Peppiatt, C.M., Howarth, C., Mobbs, P., and Attwell, D. (2006). Bidirectional control of CNS capillary diameter by pericytes. Nature *443*, 700–704.

Raichle, M.E., and Mintun, M.A. (2006). Brain work and brain imaging. Annu. Rev. Neurosci. *29*, 449–476.

Rungta, R.L., Osmanski, B.-F.F., Boido, D., Tanter, M., and Charpak, S. (2017). Light controls cerebral blood flow in naive animals. Nat. Commun. *8*, 14191.

Segal, S.S., and Duling, B.R. (1986). Communication between feed arteries and microvessels in hamster striated muscle: segmental vascular responses are functionally coordinated. Circ. Res. *59*, 283–290.

Shepherd, G.M. (2003). The Synaptic Organization of the Brain (Oxford University Press).

Stevens, B., Porta, S., Haak, L., Gallo, V., and Fields, R.D. (2002). Adenosine: a neuron-glial transmitter promoting myelination in the CNS in response to action potentials. Neuron *36*, 855–868.

Tian, P., Teng, I.C., May, L.D., Kurz, R., Lu, K., Scadeng, M., Hillman, E.M., De Crespigny, A.J., D'Arceuil, H.E., Mandeville, J.B., et al. (2010). Cortical depth-specific microvascular dilation underlies laminar differences in blood oxygenation level-dependent functional MRI signal. Proc. Natl. Acad. Sci. USA *107*, 15246–15251.

Tiret, P., Chaigneau, E., Lecoq, J., and Charpak, S. (2009). Two-photon imaging of capillary blood flow in olfactory bulb glomeruli. Methods Mol. Biol. *489*, 81–91.

Tykocki, N.R., Boerman, E.M., and Jackson, W.F. (2017). Smooth muscle ion channels and regulation of vascular tone in resistance arteries and arterioles. Compr. Physiol. *7*, 485–581.

Uhlirova, H., Kılıç, K., Tian, P., Thunemann, M., Desjardins, M., Saisan, P.A., Sakadžić, S., Ness, T.V.V., Mateo, C., Cheng, Q., et al. (2016). Cell type specificity of neurovascular coupling in cerebral cortex. eLife *5*, 5.

Vanlandewijck, M., He, L., Mäe, M.A., Andrae, J., Ando, K., Del Gaudio, F., Nahar, K., Lebouvier, T., Laviña, B., Gouveia, L., et al. (2018). A molecular atlas of cell types and zonation in the brain vasculature. Nature *554*, 475–480.

Wachowiak, M., and Cohen, L.B. (2001). Representation of odorants by receptor neuron input to the mouse olfactory bulb. Neuron *32*, 723–735.

Wei, H.S., Kang, H., Rasheed, I.D., Zhou, S., Lou, N., Gershteyn, A., McConnell, E.D., Wang, Y., Richardson, K.E., Palmer, A.F., et al. (2016). Erythrocytes are oxygen-sensing regulators of the cerebral microcirculation. Neuron *91*, 851–862.

Welsh, D.G., Tran, C.H.T., Hald, B.O., and Sancho, M. (2018). The conducted vasomotor response: function, biophysical basis, and pharmacological control. Annu. Rev. Pharmacol. Toxicol. *58*, 391–410.

Yu, X., He, Y., Wang, M., Merkle, H., Dodd, S.J., Silva, A.C., and Koretsky, A.P. (2016). Sensory and optogenetically driven single-vessel fMRI. Nat. Methods *13*, 337–340.

Zhang, Z., Payne, K., and Pallone, T.L. (2014). Syncytial communication in descending vasa recta includes myoendothelial coupling. Am. J. Physiol. Renal Physiol. *307*, F41–F52.

STAR★METHODS

KEY RESOURCES TABLE

REAGENT or RESOURCE	SOURCE	IDENTIFIER
Antibodies		
Hoescht	Life Technologies	Cat#3342
Olig-2 rabbit	Millipore	Cat#AB9610
GFP chicken	Invitrogen	Cat#A10262
PDGFαR rat	BD Biosciences	Cat#558774
Anti-rabbit 550	Cliniscience	Cat#H-1000
Anti-rabbit 405	Invitrogen	Cat#A-31556
Anti-rat 633	Invitrogen	Cat#A-21094
Anti-chicken 488	Invitrogen	Cat#A11039
Chemicals, Peptides, and Recombinant Proteins		
Texas Red Dextran (70 kDa)	Molecular Probes, Thermo Fisher Scientific	Cat#D1830
Medetomidine	Orion Pharma	Domitor
Ketamine	Virbac	Ketamine 1000
Xylazine	Bayer	Rompun 2%
CaRuby-Nano Dextran (6 kDa)	Collot et al., 2015 (Jean-Maurice Mallet)	N/A
Clacium Green-1 Dextran (10 kDa)	Invitrogen	Cat#C3713
Tamoxifen	Sigma	Cat#T5648
Paraformaldehyde	Electron Microscopy Sciences	Cat#15710
Normal Goat Serum Blocking Solution	Cliniscience	Cat#S-1000
Vecatashield	Cliniscience	Cat#H-1000
Texas Red-BSA	Invitrogen	Cat#A23017
Gelatin	Sigma	Cat#G1890
Triton X-100	Sigma	Cat#T9284
Texas Red Dextran (3000 MW)	Invitrogen	Cat#D3329
D-AP5	Hello Bio	Cat#HB0225
NBQX	Hello Bio	Cat#HB0443
MPEP	Tocris	Cat#1212
CPCCOEt	Tocris	Cat#1028
LY 341495	Tocris	Cat#1209
Experimental Models: Organisms/Strains		
Mouse: NG2-CreERT2	Huang et al., 2014 (Frank Kirchhoff)	N/A
Mouse: Ai95(RCL-GCaMP6f)-D	Madisen et al., 2015 (Hongkui Zeng, Allan Institute)	See Jax Stock No: 024105
Mouse: C57BL/6	Janvier Labs	SSAL (Orléans) –1993 (F172)
Mouse: C57BL/6J-Tg(Thy1-GCaMP6f) GP5.11Dkim/J	The Jackson Laboratory	Stock No: 025339
Software and Algorithms		
MATLAB 2013	MathWorks	https://www.mathworks.com/
ImageJ	NIH	https://imagej.nih.gov/ij/
Prism	GraphPad	https://www.graphpad.com/scientific-software/prism/
LabView 2013	National Instruments	http://www.ni.com/fr-fr/shop/labview.html
Clampfit 10.7	Axon Instruments	https://www.moleculardevices.com/products/axon-patch-clamp-system

CONTACT FOR REAGENT AND RESOURCE SHARING

Further information and requests for resources and reagents should be directed to and will be fulfilled by the Lead Contact, Serge Charpak (serge.charpak@parisdescartes.fr).

EXPERIMENTAL MODEL AND SUBJECT DETAILS

All animal care and experimentation was performed in accordance with the INSERM Animal Care and Use Committee guidelines (protocol numbers CEEA34.SC.122.12 and CEEA34.SC.123.12). Adult mice (2–6 months old, 20–35 g, both males and female, housed in 12-hr light-dark cycle) were used in this study. Mice strains were obtained from the following suppliers; *C57BL/6JRj* from Janvier Labs, *Ai95(RCL-GCaMP6f)* were donated from Hongkui Zeng (Allan Institute) (Madisen et al., 2015), *NG2-CreERT2* were donated from Frank Kirchhoff (Huang et al., 2014), *Thy1-GCaMP6f (GP5.11)* purchased from Jackson laboratory. All mice were bred on a *C57BL/6* background. To generate mice with conditional GCaMP6f expression in mural cells, *NG2-CreERT2* mice were crossed with *Ai95(RCL-GCaMP6f)* mice. Mice were administered either 1 mg or 2 mg of tamoxifen for 5 or 3 consecutive days respectively. Mice used in this study were heterozygous for cre, and either heterozygous or homozygous for GCaMP6f. Chronic craniotomies were performed as previously described (Rungta et al., 2017).

METHOD DETAILS

Surgery and Anesthesia

In brief, mice were initially anesthetized with an intraperitoneal (IP) bolus of ketamine-xylazine (100 mg kg^{-1} and 10 mg kg^{-1} body mass, respectively) or ketamine-medetomidine (100 mg kg^{-1} and 0.4 mg kg^{-1} body mass, respectively). Further 10%–20% of the same mixture was injected IP as necessary to maintain surgical plane anesthesia. During surgery, the mice breathed a mixture of air and supplementary oxygen and the body temperature was monitored with a rectal probe and maintained at ~36.5°C by a feedback-controlled heating pad. A craniotomy was performed with a dental drill and care taken not to apply pressure to the bone and the area was regularly flushed with cool aqueous buffer solution to avoid damage or heating of the underlying tissue. A cover glass (100 μm thick) was used for the window and sealed in place with photopolymerizable dental cement, which was also used to form a head-cap in which a titanium head-bar was embedded. Mice were permitted to recover for at least 3 weeks before the experimental sessions began.

For anesthetized chronic experiments, mice were anesthetized with ketamine-xylazine (100 mg and 10 mg kg^{-1} body mass, respectively) or ketamine-medetomidine (100 mg kg^{-1} and 0.4 mg kg^{-1} body mass, respectively) injected IP; no differences were observed between groups and data were pooled. Experiments were performed within 20–100 min following injection of anesthetics. Breathing rate (2–3 Hz, regular and rhythmic) was monitored with a pneumogram transducer (Biopac Systems). Body temperature was maintained at ~36.5°C–37°C using a heating pad.

For acute pharmacology experiments, the same anesthetic protocol was used. The craniotomy was drilled over the left olfactory bulb and the dura was removed. Agar (2%) was used to cover the craniotomy and mice were immediately transferred to the experimental setup.

Immunohistochemistry

Anesthetized mice were perfused transcardially with 20 mL of PBS followed by 20 mL of 4% paraformaldehyde (PFA) at room temperature. Olfactory bulbs were removed and left in 4% PFA overnight. Bulbs were sliced in coronal sections of 50-100 μm. Immunostaining went as follows: 1) Pre-incubation in 4% NGS (S-1000, Cliniscience) and 1% Triton (Sigma) for 1 day. 2) Slices were bathed in 2% NGS and 0.2% Triton containing primary antibodies at various dilutions for 3 days at 4°C. 3) Slices were washed 4 times with PBS for 5-10 min followed by addition of secondary antibodies in 2% NGS for >4 hr at room temperature. For slices stained with Hoescht antibody, it was added for 5 min after secondary antibodies. 4) Slices were washed 4 times with PBS for 5-10 min and then mounted in Vecatashield (H-1000, Cliniscience) for confocal microscopy (Zeiss LSM-510). The following primary and secondary antibodies were used: Olig-2 rabbit (AB9610, Millipore), 1:200; GFP chicken (A10262, Invitrogen), 1:1000; PDGFαR rat (558774, BD Biosicences), 1:100; anti-rabbit-550 (AS111782, Cliniscience) 1:500; anti-rabbit-405 (Invitrogen) 1:500; anti-rat-633 (Invitrogen); anti-chicken-488 (A11039, Invitrogen) 1:500; Hoeschst (3342, Life technologies) 1:2000. In order to stain the vessel lumen (Figure S1A), PFA perfusion was directly followed by perfusion of 2 mg of Texas Red-BSA (A23017, Invitrogen) and 2 mg of Gelatin (G1890, Sigma) dissolved in PBS at 37°C, the mouse was then placed on ice for 2 min prior to extraction of the olfactory bulbs.

Nose Loading

Mice were anesthetized with an IP injection of ketamine (100 mg/kg) and xylazine (10 mg/kg). CaRuby-Nano dextran (6 kDa) (Collot et al., 2015) or Calcium Green-1 dextran (10 kDa, Molecular Probes) was dissolved 2.5% wt/vol in a solution of PBS with 0.2% Triton X-100 (Sigma-Aldrich). 8 μL of this solution was injected in the mouse naris using a cannula inserted 9–10 mm, and mice were left on their backs to recover from anesthesia on a heating pad with supplemental oxygen. This resulted in the uptake and transport of the

dye by olfactory sensory neurons (OSNs) to their terminals in individual glomeruli as previously described (Otsu et al., 2015; Wachowiak and Cohen, 2001). Imaging of OSN terminal Ca^{2+} was performed 3-12 days following loading protocol.

Two-Photon Laser Scanning Microscopy

Imaging was performed using a femtosecond laser (Mai Tai eHP; SpectraPhysics) with a dispersion compensation module (Deepsee; Spectraphysics) emitted ~70-fs pulses at 80 MHz. Laser power was attenuated by an acoustic optical modulator (AA Optoelectronic, MT110-B50-A1.5-IR-Hk). XY scanning was performed with Galvanometric scanner (GS) mirrors (8315KM60B; Cambridge Technology). GCaMP6f, Texas Red and Ca-Ruby were excited at 920 nm. Emitted light was collected with either a 60X/1.10NA (Olympus) or 40X/0.8NA (Leica) water immersion objective and was sent to a pair of lenses, coupled into a 2-mm diameter core polymethyl methacrylate optical fiber. Collected light was split using a dichroic mirror at 580 nm and the signals were each detected with a dedicated GaAsP photomultiplier tube (Hamamatsu) after passing through an appropriate emission filter (GCaMP6f: 525 nm, 50 nm bp; Texas Red, Ca-Ruby: 620 nm, 60 nm bp). Customized Labview software was used to control imaging parameters. Texas Red dextran (70 kDa, Molecular Probes) was administered intravenously by retro-orbital injection. For example images in figures displaying pericyte-GCaMP6f surrounding capillaries in which single RBCs are visible, the GCaMP6f signal was averaged over several frames, whereas the Texas-Red image represents a single frame. For awake experiments, mice were briefly (<2 min) anesthetized with isoflurane in order to inject the Texas Red dextran and recovered for >1.5 hr before the experimental session began.

Sensory Stimulation

A home built olfactometer based on the design of the Rinberg lab (https://www.janelia.org/open-science/olfactometer), and controlled by custom Labview software was used to deliver the odors. Pure air was constantly delivered to the mouse nose and a valve switched the flow from air to an odor-air mixture (800 mL min^{-1}) for a 2 s stimulation. The pressure of the air line and the odor line were measured and balanced before starting the experiment. Odor concentrations were calibrated with a photo-ionization detector (miniPID 200B, Aurora Scientific, Aurora, Canada). The air plus odor mixture was supplemented with 200 mL min^{-1} O_2. For awake mice total air flow was 500 mL min^{-1} of odor-air mixture with no additional O_2.

Pharmacology

Pipette solution contained in mM; NaCl, 125; KCl, 5; Glucose, 10; HEPES, 10; $CaCl_2$, 2; $MgSO_4$, 2; Texas-Red dextran, 0.007 ± the following blockers: D-APV, 500 μM; NBQX, 300 μM; MPEP, 250 μM; CPCCOEt, 500 μM; LY341495, 100 μM. A multichannel pressure injector (PM 8000, MDI) was used to inject the solution into the targeted glomerulus via a glass micropipette and successful injection was visualized by spread of Texas-Red fluorescence. Drugs were washed out for 12-25 min, except for in one experiment in which the washout was not attempted.

Awake Imaging

Mice were head-fixed to a frame with a running wheel as shown in Figure 7A. Mice were gradually habituated to the experimental setup and the regular delivery of odors for >5 days before experimental sessions began. Locomotion and movement were monitored with a velocity encoder connected to the running wheel and a camera with the IR filter removed. Only trials where the mouse stayed still throughout the odor delivery were analyzed.

Mathematical Modeling

A detailed description of the model is described in Data S1. The following input parameters were used: P_{Pia} = 80 mmHg. Diameter (Figure 6A): Median values of paired measurements in all compartments (juxta-synaptic capillaries to upstream parenchymal arteriole). The pial diameter was estimated using the ratio of paired pia/arteriole diameter changes from separate experiments. Length and branching of each compartment are provided as a table at the end of Data S1.

QUANTIFICATION AND STATISTICAL ANALYSIS

Ca^{2+} signals were calculated as $\Delta F/F = (F - F_0) / F_0$, where F_0 represents baseline fluorescence and F the fluorescence at time t ($F_{background}$ not subtracted). Glomeruli OSN terminal Ca-Ruby signals were considered positive when the mean $\Delta F/F$ (over 3 s following the odor onset) > 2SD of the baseline. The magnitude of the OPC Ca^{2+} signal plotted in Figure 1G represents the mean $\Delta F/F$ calculated over 3 s following the odor onset. Pericyte Ca^{2+} transients were analyzed in Clampfit 10.7 (Axon Instruments), with a detection threshold of 3SD from the local baseline for >100 ms. A 50 ms temporal running average filter was applied to Ca^{2+} signals from line scan acquisitions to reduce noise, all plotted points represent the mean of the preceding 50 ms. Quantification of resting Ca^{2+} was made in trials with well separated transients, the traces were further filtered with a 1 Hz low-pass Gaussian filter and the minimum values were compared during baseline and a 5 s period from the end of the odor application. Lumen diameters were measured with line scans perpendicular to and crossing the vessel and calculated using the fluorescent boundaries of the Texas Red (70 kDa) fluorescence, which labels the blood plasma (excluding the glycocalyx). A 200 ms mean filter (preceding time, t) was used, and fluorescence was interpolated between pixels on the distance axis. Red blood cells were imaged as shadows within the fluorescent plasma and their velocity was calculated based on the distance traveled per unit of time. A detailed explanation of the

methodology to calculate RBC velocity is provided as Data S2 along with Video S5. Calcium, diameter, and velocity measurements from individual mice represent average responses from 3 to >15 trials. Averaging was particularly necessary for velocity measurements in arterioles and capillaries close to the arteriole due baseline fluctuations caused by pulsatility (see single trial from pial arteriole in Video S5). For statistical comparisons between groups a paired Student's t test was performed, except for Figure 1G which did not pass the shapiro-wilk normality test and a Mann-Whitney test was performed. For all statistical comparisons normality was assessed with a shapiro-wilk normality test except for Figure 4D in which the n was too small (n of 5), and normality was assumed from the larger dataset of Ca^{2+} transient frequencies in Figure 3G which passed the shapiro-wilk normality test. For assessing onset delays between mouse averaged OSN-CaRuby and OPC-GCaMP6f signal, onset $\geq$ 2SD of baseline for $\geq$ 25 ms, normality was assumed and a one sample t test was performed against a theoretical mean of 0.0. In Figure 2C, a one-way ANOVA was performed, with Turkey's multiple comparison test. ****,***, **, and * indicate $p < 0.0001$, 0.001, 0.01 and 0.05 respectively. Data throughout the paper is displayed as the mean ± SEM. Paired experiments were interleaved, no randomization or blinding was used. No statistical methods were used to predetermine sample sizes. One mouse in which the first order vessel dilated slower than the arteriole was shown separately in Figure S7E and was not grouped with the data in Figures S7A–S7C. No mice were excluded from this paper.

Neuron, Volume *99*

Supplemental Information

Vascular Compartmentalization of Functional Hyperemia from the Synapse to the Pia

Ravi L. Rungta, Emmanuelle Chaigneau, Bruno-Félix Osmanski, and Serge Charpak

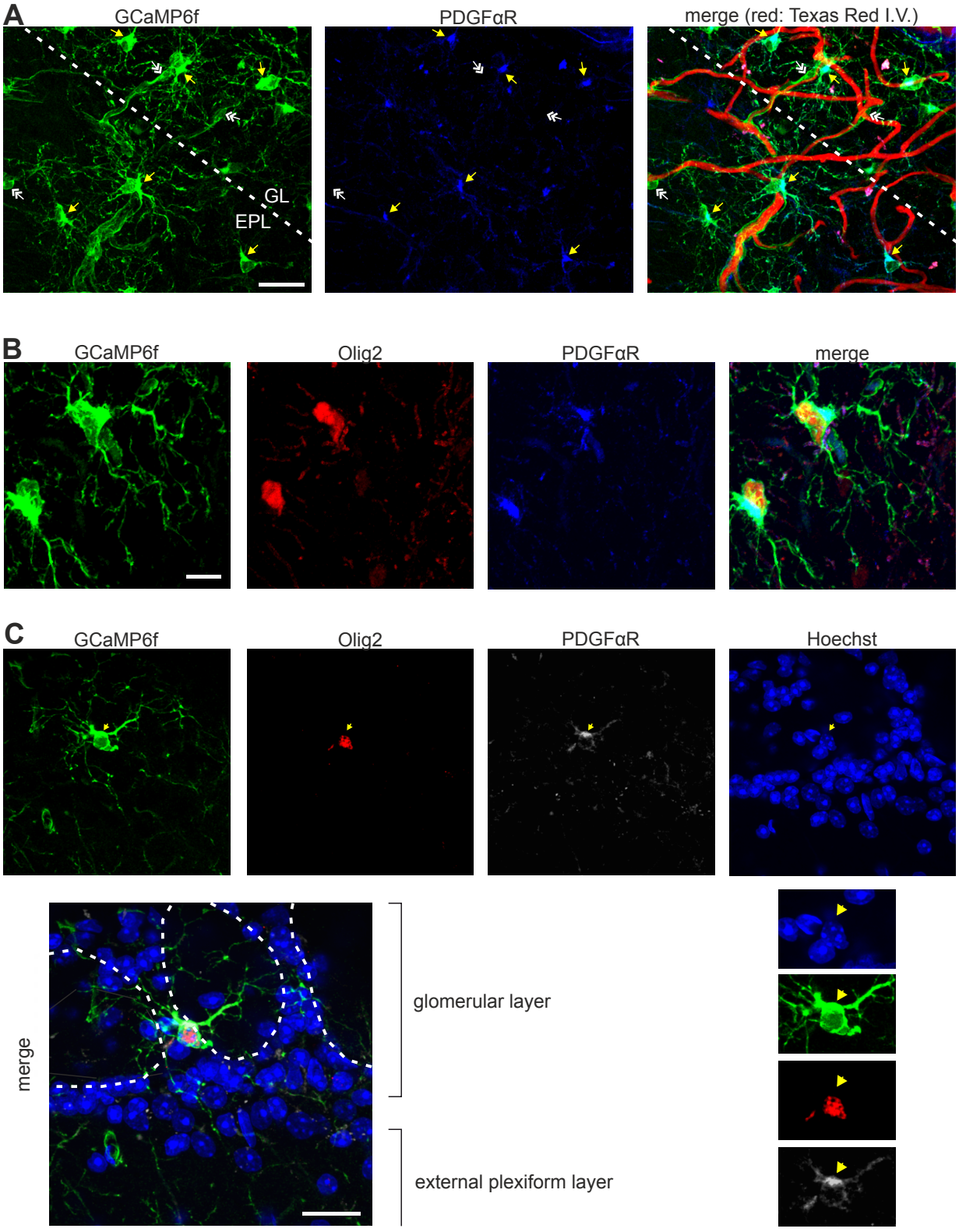

Figure S1. Immunostaining indicates GCaMP6f expression in olfactory bulb OPCs. Related to Figure 1.

(**A**) Single yellow arrows point to OPCs that express GCaMP6f (green) and are positive for

PDGFαR (blue). Double white arrows point to capillary pericytes that express GCaMP6f (green), are negative for PDGFαR (blue), and are found on capillaries (red). Glomerulus layer (GL) and External Plexiform layer (EPL) are separated by dashed white line. Stack size: 18 μm z-projection, scale bar: 25 μm. (**B**) Triple staining shows that GCaMP6f expressing OPCs are positive for both Olig2 and PDGFαR. Stack size: 16 μm z-projection, scale bar: 10 μm. (**C**) Hoechst (blue) indicates location of periglomerular nuclei allowing identification of glomeruli boundaries (dashed white lines encircle individual glomeruli). Olig2 and PDGFαR staining indicate that the GcAMP6f expressing cell is an OPC and it extends processes into more than 1 glomeruli. Yellow arrow indicates typical nuclear expression of Olig2 that does not overlap with surrounding PDGFαR staining. Stack size: 5 μm z-projection, scale bar: 20 μm.

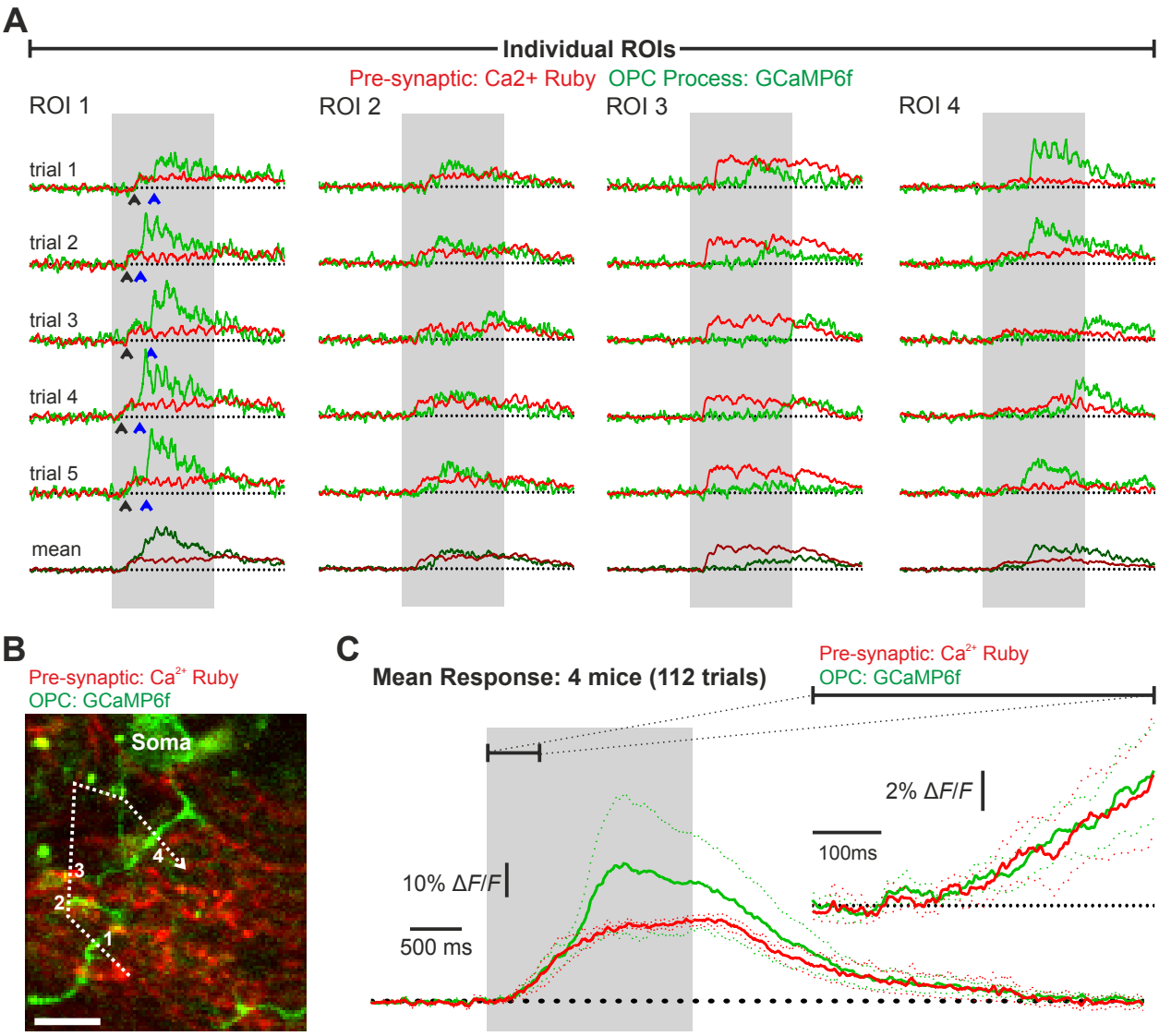

Figure S2. Odor stimulation evokes biphasic Ca^{2+} elevations in glomerular OPC processes. Related to Figure 1.

(A) 5 consecutive trial by trial responses (top) and mean of 5 trials (bottom) showing OSN pre-synaptic Ca^{2+} elevation (red) and adjacent OPC process Ca^{2+} elevation (green) in individual ROIs numbered 1-4 in (**B**). Grey shaded area indicates timing of a 2 second odor application. ROI 1 consistently shows a rapid OPC process signal synchronous with the presynaptic Ca^{2+} elevation (black arrowhead), and a secondary increase which is delayed (blue arrowhead). In ROIs 2-4 the first OPC Ca^{2+} elevation is barely detectable, but the secondary elevation consistently occurs with a varying delay. (**B**) Mean image taken from a time series during an odor application shows presynaptic labeling (red) and OPC-GCaMP6f (green). Dashed line shows path of line scan. Scale bar: 5 µm. (**C**) Mean response of paired pre-synaptic and OPC process Ca^{2+} signals shows that the onset of the pre-synaptic Ca-Ruby signal and the OPC GcAMP6f signal were indistinguishable in response to a natural odor stimulation. Right inset shows expanded traces from between the hash marked line. Data represents mean (solid lines) ± SEM (dashed lines).

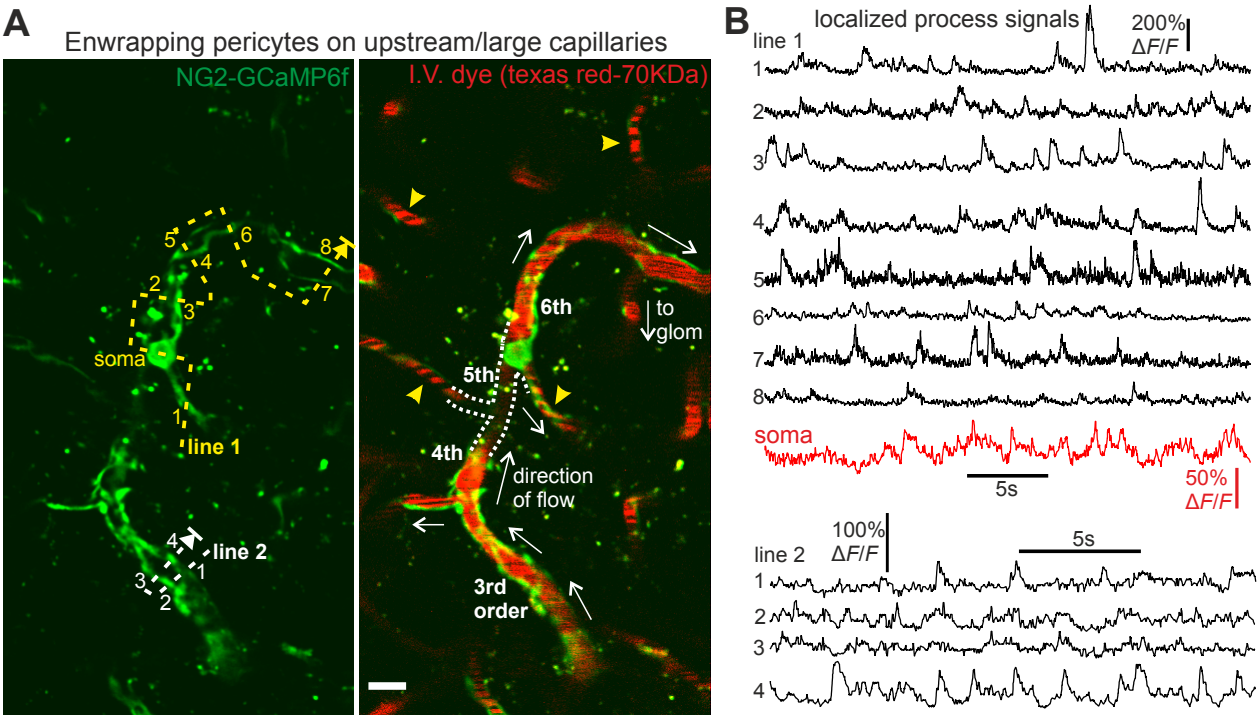

Figure S3. Microdomain Ca^{2+} transients in enwrapping-type pericyte processes. Related to Figure 3 and Movie S3.

(**A**) Single z-plane image shows GCaMP6f fluorescence (green) in enwrapping type pericytes on capillaries located in the external plexiform layer (EPL) and upstream from a glomerulus. These capillaries are larger than downstream glomerulus capillaries that are contacted by thin-strand pericytes as well as surrounding capillaries in the same field of view (yellow arrows, right). Left: Yellow and white dashed arrows lines indicates the path of 2 broken line scans plotted in (B) on the 2 different branches. Right: White dashed line indicates the path of the capillary that dips below the imaged z-plane. White arrows indicate direction of blood flow, which was followed forwards to a glomerulus located above the imaged z plane. (**B**) As in the thin strand pericyte (Figure 3), enwrapping or mesh-type pericytes also show spontaneous Ca^{2+} transients that are spatially localized. Scale bar: 10 µm. Note, different $\Delta F/F$ and time scales were used for the data plots of the 2 line scans and the soma (red).

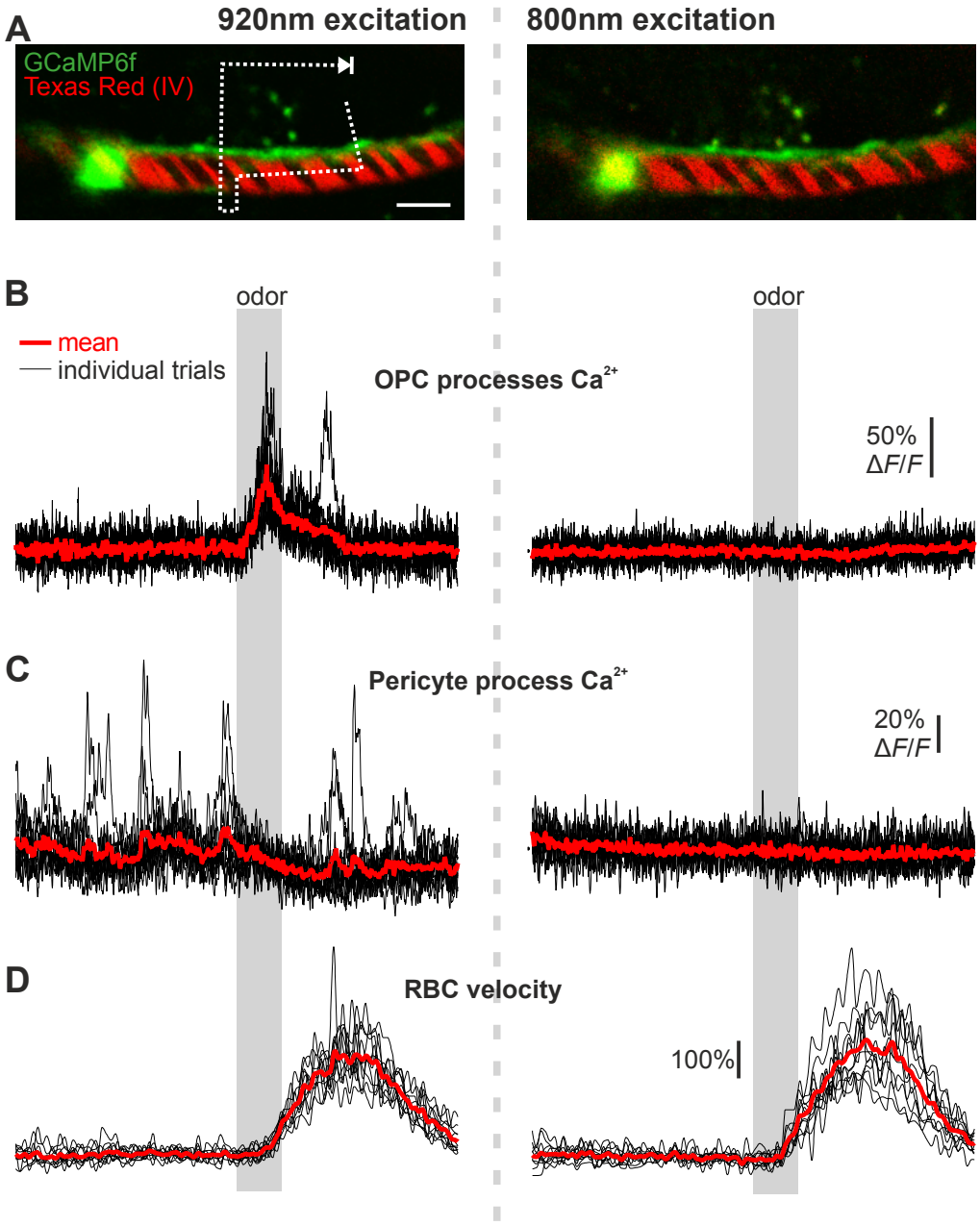

Figure S4. Imaging of GCaMP6f at different wavelengths confirms that activity dependent changes in pericyte Ca^{2+} are real and not due to volume changes. Related to Figures 3 and 4. (**A**) Single z-plane images of GCaMP6f (green) and Texas Red (red) fluorescence excited at 920nm (left) and 800nm (right), shows that the fluorophores can be excited at both wavelengths. Dashed line indicates path of broken line scan quantified in (B-D) to capture OPC process Ca^{2+}, pericyte process Ca^{2+} and RBC velocity simultaneously. Scale bar: 5 µm. (**B**) Imaging with 920nm excitation (left) shows that the glomerulus is activated, as indicated by an increase in OPC process GCaMP6f fluorescence. Imaging at 800nm excitation confirms that GCaMP6f sensitivity is lost at this wavelength as no increase in OPC process Ca^{2+} is observed across multiple trials. (**C**) Synaptic activation decreases frequency of transients and steady state GCaMP6f fluorescence within the pericyte process when imaged at 920nm but not 800nm, indicating that the transients

and decrease in fluorescence are indeed Ca^{2+} dependent. (**D**) RBC velocity increases consistently across multiple trials at both wavelengths. 11 individual trials were performed and are plotted at each 800nm and 920nm. The Ca^{2+} dependency of the GCaMP6f 2-photon excitation spectrum can be found at https://www.janelia.org/lab/harris-lab-apig/research/photophysics/two-photon-fluorescent-probes

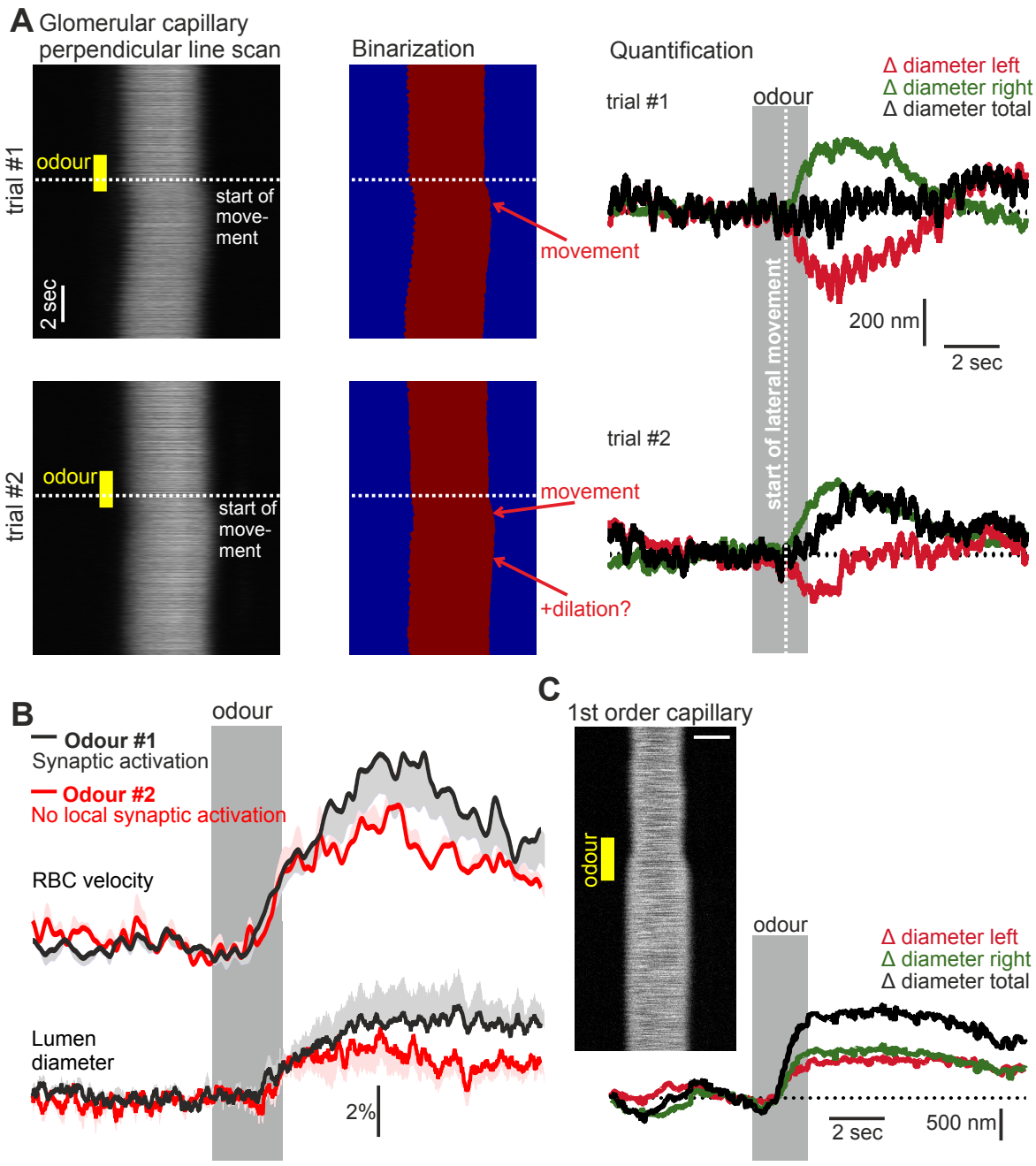

Figure S5. Lumen diameter changes of juxta-synaptic glomerulus capillaries are difficult to interpret and occur in the absence of local synaptic activation and pericyte Ca^{2+} changes. Related to Figures 3 and 4.

(**A**) Two individual trials from the same glomerulus capillary shows that the capillary moves laterally following synaptic activation. In trial #1 (top) the increase in diameter on the right is mostly matched by the decrease in diameter on the left indicating a case where dilation is not detected. In trial #2 (bottom), the increase on the right is initially matched by a decrease on the left, however, the increase on the right continues in the absence of a further decrease on the left and results in the detection of a delayed diameter increase that is unilateral and difficult to interpret. Note, individual RBCs are not visible in the left images because of the compressed time scale. (**B**)

RBC velocity (top, same data from Figure 4C) with quantified lumen diameter changes (bottom), shows that when the lumen diameter is analyzed, the increase in RBC velocity is accompanied by a small increase in diameter. Although these diameter changes were not interpreted, if they were indeed real, the observation that they occurred independently of local synaptic activity or decreases in pericyte Ca^{2+} (red traces, see Figure 4C), suggests that they were passive. n=5 paired experiments from 5 mice. Decreases in diameter were never detected. Data represents mean ± SEM. (**C**) An example of a diameter increase (single trial) at the level of a 1st order capillary, upstream of an activated glomerulus (Example mouse #2, Figure S6), that shows an unambiguous dilation. Scale bar: 5 μm.

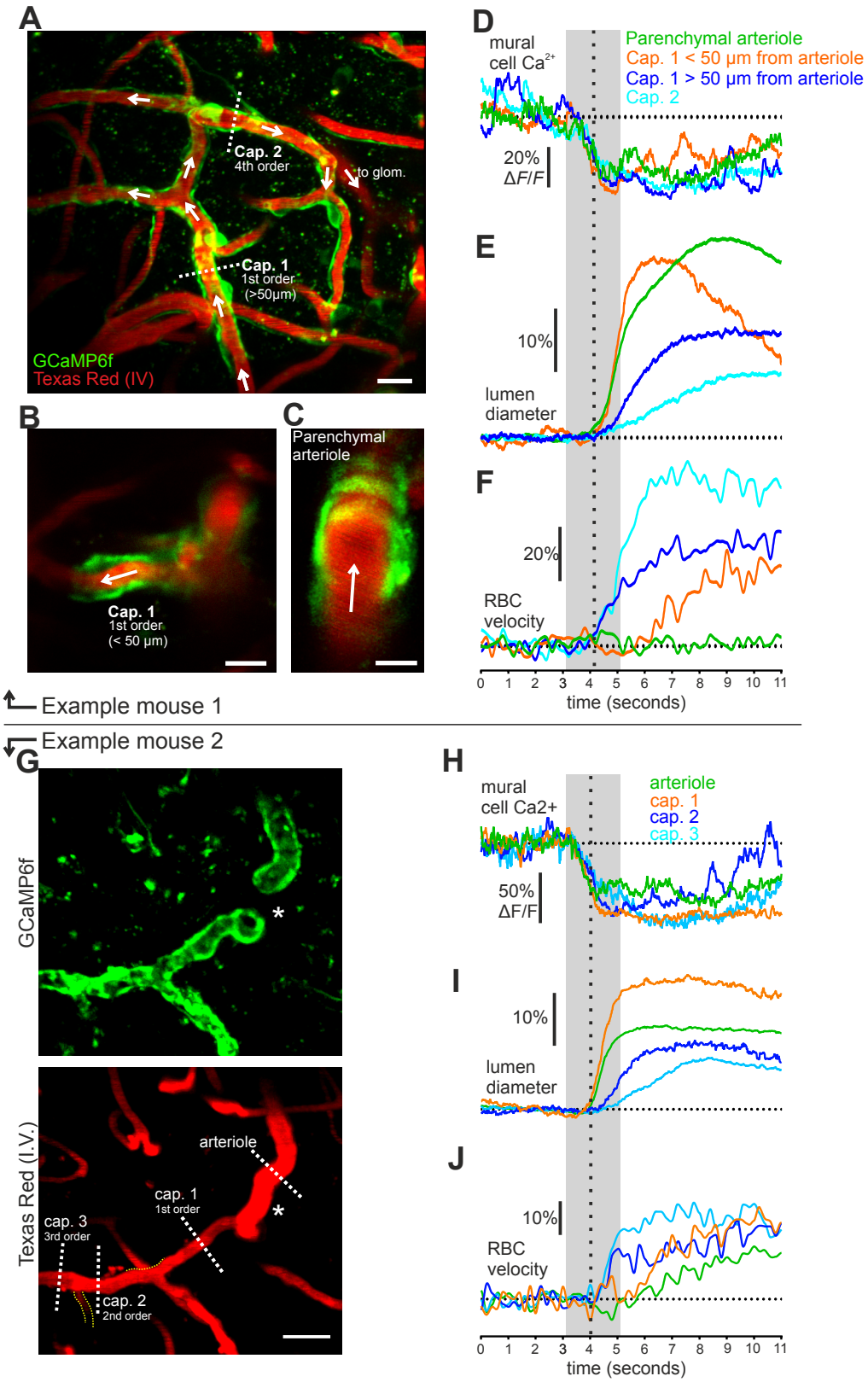

Figure S6. Individual examples of hemodynamics and mural cell Ca^{2+} signaling upstream of an activated glomerulus. Related to Figure 5.

This figure shows data obtained from individual vascular networks. (**A**) 50 µm z-stack max

projection showing GCaMP6f expressing (mesh type) pericytes that are enwrapping capillaries upstream of a glomerulus and > 50 µm downstream of the arteriole. Scale: 20 µm (**B**) single z plane image of the first capillary branch point off of the feeding arteriole. Scale: 10 µm (**C**) 5 µm z-stack max projection showing GCaMP6f expressing SMCs covering the arteriole. Scale: 10 µm. Arrows indicate the direction of RBC flow. (**D**) The Ca^{2+} drop in all mural cells. (**E**) Dilation occurs first and simultaneously in arteriole and the proximal portion of the 1st order capillary and becomes progressively delayed with distance downstream. Note, the speed of the dilation is not dependent on branch order as the portion of the first order capillary furthest from the arteriole dilates more slowly (blue trace). (**F**) The increase in RBC velocity occurs first in the downstream capillaries that dilate more slowly and is delayed in the proximal portion of the capillary. In this example the arteriole RBC velocity remains constant. (**G**) 47 µm z stack max projection showing GCaMP6f expression (top) and Texas Red fluorescence in lumen (bottom) along the arteriole and 1st-3rd order capillaries upstream of an activated glomerulus. Yellow dashed lines show the location of the vessel when it dips out of the focal plane or crosses over a non-connected vessel. Star indicates portion of the arteriole negative for GCaMP6f expression (**H**) Synchronous Ca^{2+} drop in all mural cells. (**I**) Dilation occurs first and simultaneously in arteriole and proximal portion of the capillary and becomes progressively delayed with distance. (**J**) The increase in RBC velocity occurs first in the downstream capillaries that dilate more slowly and is delayed in the proximal portion of the capillary and the arteriole. Dashed white lines indicate the location of the diameter measurements. Dashed vertical lines on traces serve as visual cue to compare timing of events. Grey shaded region represents odor delivery. Traces represent averages of 4-13 trials.

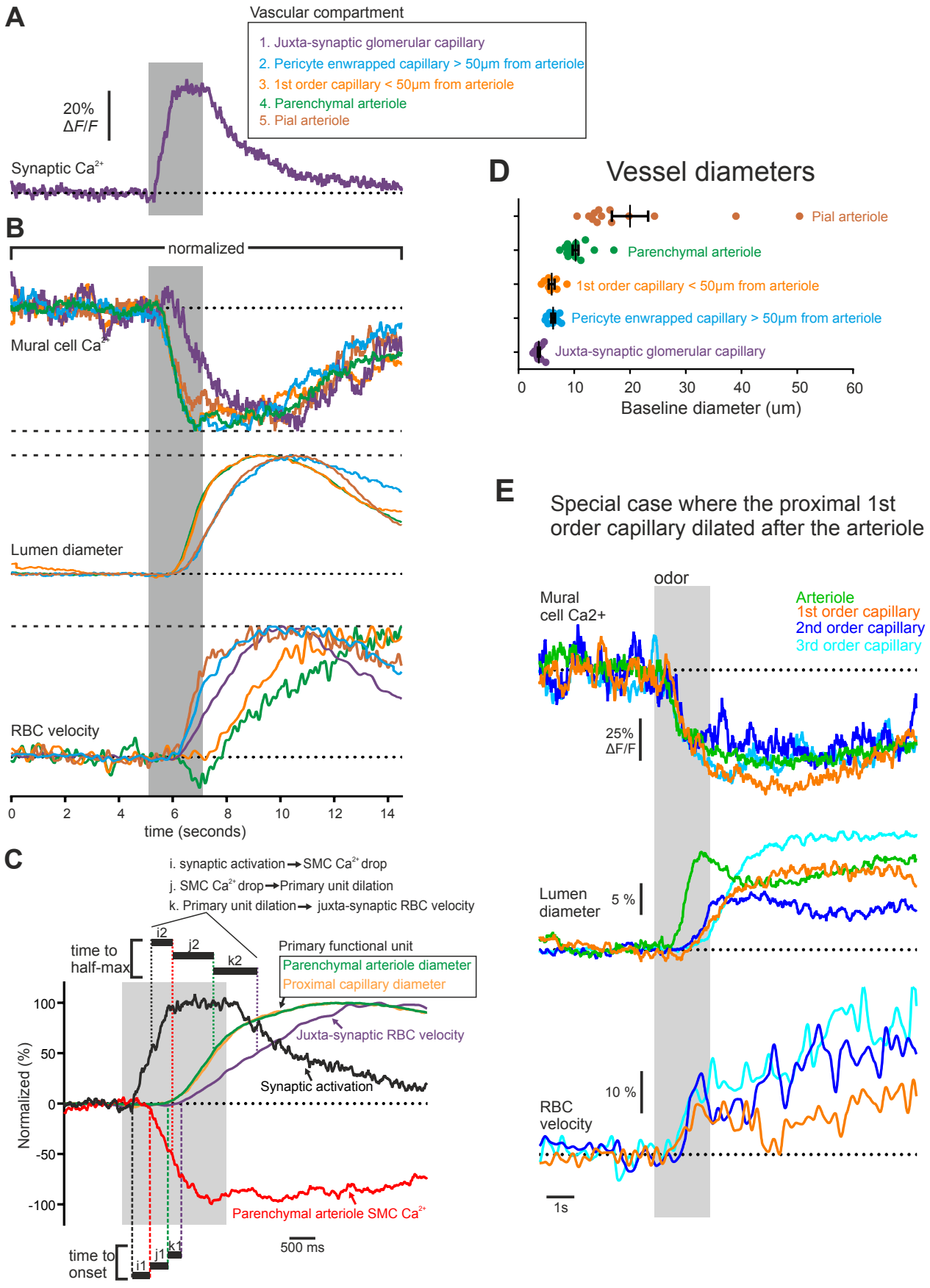
A
Vascular compartment
1. Juxta-synaptic glomerular capillary
2. Pericyte enwrapped capillary > 50µm from arteriole
3. 1st order capillary < 50µm from arteriole
4. Parenchymal arteriole
5. Pial arteriole
20% ΔF/F
Synaptic Ca2+
B
normalized
Mural cell Ca2+
Lumen diameter
RBC velocity
0 2 4 6 8 10 12 14
time (seconds)
C
i. synaptic activation → SMC Ca2+ drop
j. SMC Ca2+ drop → Primary unit dilation
k. Primary unit dilation → juxta-synaptic RBC velocity
time to half-max
i2
j2
k2
Primary functional unit
Parenchymal arteriole diameter
Proximal capillary diameter
Juxta-synaptic RBC velocity
Synaptic activation
Parenchymal arteriole SMC Ca2+
Normalized (%)
100
50
0
-50
-100
time to onset
i1
j1
k1
500 ms
D
Vessel diameters
Pial arteriole
Parenchymal arteriole
1st order capillary < 50µm from arteriole
Pericyte enwrapped capillary > 50µm from arteriole
Juxta-synaptic glomerular capillary
0 10 20 30 40 50 60
Baseline diameter (um)
E
Special case where the proximal 1st order capillary dilated after the arteriole
odor
Mural cell Ca2+
Arteriole
1st order capillary
2nd order capillary
3rd order capillary
25% ΔF/F
Lumen diameter
5 %
RBC velocity
10 %
1s

Figure S7. Timing of Ca^{2+} signaling and hemodynamics from the synapse to the pia: all measurements combined and one special case. Related to Figure 5.

This supplemental figure serves as an extension to Figure 5. Here the average data from all vessels recorded in this study are combined (**A**) Average timing of the synaptic response (OSN or OPC process Ca^{2+} signal). (**B**) Mean data normalized showing from top to bottom; mural cell Ca^{2+}, lumen diameter and RBC velocity at different vascular compartments. (**C**) Timing of synaptic activation, parenchymal arteriole SMC Ca^{2+} decrease, primary functional unit dilation and resulting RBC velocity increase at the synapse. Black bars and dashed vertical lines indicate the time to half-maximum (top), and the time to onset (bottom). Data in (**A-C**) represents multiple branches from 23 distinct vascular networks in 17 mice. Glomerulus capillary, n= 14; Enwrapped > 50 μm from arteriole, n=10; Enwrapped <50 μm from arteriole, n=8; arteriole, n=18; Pial arteriole, n=13. (Every vascular compartment was not imaged in each vascular network, RBC velocity was only measured in a subset of branches, and in a few cases Ca^{2+} was not measured at all branches due to sparseness of GCaMP6f expression). Data incorporated into (**A-C**) was also presented in Figures 3-5. (**D**) Distribution of baseline diameters for each vessel type. Data represents mean ± SEM. **(E)** Analysis of a case where the proximal 1st order capillary dilated after the arteriole. Top, Arteriole SMC and pericyte (1st to 3rd order capillaries) show "synchronous" Ca^{2+} decreases. Middle, Arteriole dilates before all capillary branch orders. Bottom, RBC velocity increases fast in all capillary branch orders. Vessels were traced backwards from a capillary in an activated glomerulus. Data represents averages of 3-4 trials. Note, Arteriole RBC velocity was not measured as the vessel was never horizontal with the 2D imaging plane.